

1 **Multi-instrument observations of Meso-Scale**
2 **enhancement of Sub-Auroral Polarization Stream**
3 **associated with an injection**

4 **Zihan Wang¹, Shasha Zou¹, Simon G. Shepherd², Jun Liang³, Jesper W.**
5 **Gjerloev⁴, J. Michael Ruohoniemi⁵, Bharat Kunduri⁵, and John R. Wygant⁶**

6 ¹Department of Climate and Space Sciences and Engineering, University of Michigan, Ann Arbor, MI,
7 United States

8 ²Thayer School of Engineering, Dartmouth College, Ann Arbor, MI, United States

9 ³Department of Physics and Astronomy, University of Calgary, Calgary, Alberta, Canada

10 ⁴Applied Physics Laboratory Johns Hopkins, Laurel, MD, United States

11 ⁵Virginia Polytechnic Institute and State University, Blacksburg, VA, United States

12 ⁶University of Minnesota, School of Physics and Astronomy, Minneapolis, MN, United States

13 **Key Points:**

- 14 • Meso-scale enhancement of SAPS observed by VAP and SuperDARN embedded
15 in the existing large-scale SAPS.
16 • Meso-scale enhancement of SAPS is associated with energetic ion flux increase,
17 energetic electron flux decrease, and local magnetic field dip.
18 • Meso-scale enhancement of SAPS and equatorward flow burst develop near the
19 Harang reversal.

This is the author manuscript accepted for publication and has undergone full peer review but has not been through the copyediting, typesetting, pagination and proofreading process, which

may lead to differences between this version and the Version of Record. Please cite this article as doi: [10.1029/2019JA026535](https://doi.org/10.1029/2019JA026535)

Abstract

Sub-Auroral Polarization Streams (SAPS) prefer geomagnetically disturbed conditions and strongly correlate with geomagnetic indexes. However, the temporal evolution of SAPS and its relationship with dynamic and structured ring current and particle injection are still not well understood. In this study, we performed detailed analysis of temporal evolution of SAPS during a moderate storm on May 18, 2013 using conjugate observations of SAPS from the Van Allen Probes (VAP) and the Super Dual Auroral Radar Network (SuperDARN). The large-scale SAPS (LS-SAPS) formed during the main phase of this storm and decayed due to the northward turning of the interplanetary magnetic field (IMF). A meso-scale (\sim several hundreds km zonally) enhancement of SAPS was observed by SuperDARN at 0456 UT. In the conjugate magnetosphere, a large SAPS electric field (~ 8 mV/m) pointing radially outward, a local magnetic field dip and a dispersionless ion injection were observed simultaneously by VAP-A at L shell=3.5 and MLT=20. The particle injection observed by VAP-A is likely associated with the particle injection observed by the Geostationary Operational Environmental Satellite (GOES) 15 near 20 MLT. Magnetic perturbations observed by the ground magnetometers and flow reversals observed by SuperDARN reveal that this meso-scale enhancement of SAPS developed near the Harang reversal and before the substorm onset. The observed complex signatures in both space and ground can be explained by a two-loop current wedge (2LCW) generated by the perturbed plasma pressure gradient and the diamagnetic effect of the structured ring current following particle injection.

1 Introduction

Sub-auroral polarization streams (SAPS) refer to high-speed westward convection flows (> 100 m/s) in the sub-auroral ionosphere extending from the afternoon to the early morning sector, and can span $3^\circ - 5^\circ$ in latitude (Foster & Vo, 2002; Kunduri et al., 2017). In the equatorial magnetosphere, SAPS correspond to large electric fields pointing radially outward from the center of the Earth, and are usually observed between the ion and electron plasma sheet inner boundaries and near the plasmopause (e.g. Califf et al., 2016; Kim, Mozer, Lee, & Jin, 2010; Nishimura et al., 2008).

There are a few proposed mechanisms for the formation of SAPS. The current generator theory works as follows (Anderson et al., 1993; Southwood & Wolf, 1978). When the convection increases in the equatorial magnetosphere, a partial ring current can build up on the night side with large azimuthal pressure gradient. This azimuthal pressure gradient together with the gradient of the magnetic field flux tube volume in the radial direction can generate the Region-2 field-aligned currents (FACs) through $j_{\parallel} \propto [(\nabla V)_{radial} \times (\nabla P)_{azimuthal}] \cdot \hat{b}$ (Vasyliunas, 1970). In the above equation, V is the flux tube volume, P is the plasma thermal pressure and \hat{b} is the direction of the magnetic field. On the dusk side, the Region-2 FACs flow into the ionosphere, and close through poleward Pederson current and then the Region-1 sense FACs at higher latitudes. When the Region-2 downward FACs are located earthward of the electron plasma sheet inner boundary, where the particle precipitation induced conductance is low, a large poleward electric field, i.e., SAPS, in the current closure region is needed to maintain the current continuity. Later, De Keyser (1999) proposed that the combined effect of finite gyroradius induced thermoelectric field and the background convection electric field at the front of the substorm particle injection when it reaches the plasmopause can account for the SAPS formation. In addition, Mishin and Puhl-Quinn (2007) pointed out that the short circuiting of the particle injection into the plasmasphere can explain the SAPS formation. According to their theory, when the injected particles enter the plasmopause, energetic electrons will stop, but ions will move further inward. This charge separation will give rise to the SAPS electric field.

70 Besides the dynamics in the magnetosphere, large convection flow speed and as-
71 sociated enhanced frictional heating in the ionosphere may increase the conversion rate
72 of atomic O^+ to molecular NO^+ and thus increase the recombination rate and plasma
73 loss rate. In addition, enhanced frictional heating leads to elevated ion temperature and
74 ion scale height increase and thus enhanced vertical transport (Heelis, Bailey, Sellek, Mof-
75 fett, & Jenkins, 1993). As a result of enhanced frictional heating, the density and con-
76 ductivity will further decrease, creating a positive feedback effect on the SAPS electric
77 fields (Banks & Yasuhara, 1978; Schunk, Banks, & Raitt, 1976).

78 All the above SAPS formation mechanisms suggest that SAPS should occur due
79 to enhanced earthward transport of plasma sheet plasma during geomagnetic active times.
80 Therefore, the SAPS occurrence and characteristics during geomagnetic storms and sub-
81 storms have been studied extensively using observations. F. He, Zhang, Wang, and Wan
82 (2017) show that SAPS occur after 0-1.5 h after the southward turning of interplanetary
83 magnetic field (IMF) during intense storms. In general, it is found that SAPS move to
84 lower magnetic latitudes and cover larger geomagnetic longitudes as K_p increases or Dst
85 decreases (Foster & Vo, 2002; Huang & Foster, 2007). The peak SAPS flow speed en-
86 hances and the electron density within the SAPS reduces when Dst decreases (Erickson,
87 Beroz, & Miskin, 2011). Recently, Kunduri et al. (2017) showed that the occurrence rate
88 of SAPS can reach over 80% during geomagnetic storms ($Dst < -50nT$). In addition,
89 Wang, Ridley, Lühr, Liemohn, and Ma (2008) also showed that larger cross polar cap
90 potentials are related with larger speed of SAPS, and Anderson (2004) showed that the
91 subauroral potential drop across SAPS is positively correlated with the absolute value of
92 Dst . During storm time, a couple of event studies showed that SAPS can last for more
93 than 10 hours (Burke et al., 2000; Califf et al., 2016). This is further confirmed by Lejosne
94 and Mozer (2017) using two years of Van Allen Probes data and the average lifetime of
95 SAPS was found to be 9 hours, which is comparable to the duration of the storm main
96 phase.

97 The dynamics of SAPS have been also frequently related to substorms and it has
98 been shown that they can last from 30 min to 3 hours (Anderson, Heelis, & Hanson, 1991;
99 Makarevich, Kellerman, Bogdanova, & Koustov, 2009; Puhl-Quinn et al., 2007). Based
100 on the coupled global BATSRUS MHD model and kinetic ring current model results, SAPS
101 can indeed last for 2-3 hours (Buzulukova et al., 2010; Yu et al., 2015). Although the du-
102 ration of SAPS and substorm is roughly comparable, we still do not understand the de-
103 tailed relation between substorm onset and SAPS. Observationally, SAPS have been shown
104 to occur at different phases of a substorm in different cases. Many studies reported that
105 SAPS can form in the expansion and recovery phase, lagging the substorm onset by 6-
106 30 min (Anderson, Carpenter, Tsuruda, Mukai, & Rich, 2001; Anderson et al., 1993; Karls-
107 son, Marklund, Blomberg, & Mälkki, 1998; Makarevich et al., 2011; Mishin, 2016; Puhl-
108 Quinn et al., 2007; Wang & Lühr, 2011). Anderson et al. (1993) further explained this
109 delay: after the onset, ion and electron plasma sheet boundaries need about 10 min to
110 separate and provide the low conductivity region. However, a much quicker response of
111 SAPS to the onset is later reported, from 30 sec after onset (Nishimura et al., 2008) to
112 2 min (Zou, Lyons, Nicolls, Heinselman, & Mende, 2009; Zou, Lyons, Wang, et al., 2009).
113 Zou, Lyons, and Nishimura (2012) reported that SAPS can start to form even in the growth
114 phase after the convection starts to increase, as part of the nightside Harang reversal.
115 This is consistent with the current generator theory that SAPS should be able to form
116 following the enhanced convection.

117 Most studies mentioned above found that SAPS extends over a large spatial scale
118 in the longitudinal direction, covering several hours of MLT (e.g. Clausen et al., 2012;
119 F. He et al., 2018), and very few studies (Oksavik et al., 2006) focus on meso- to small-
120 scale SAPS variations. Recent studies show that small- and meso-scale FACs (e.g. Lühr
121 et al., 2015; McGranaghan, Mannucci, & Forsyth, 2017) and meso-scale flow channels,
122 which are typically associated with streamers and SAPS (Gallardo-Lacourt et al., 2014,

2017), are both important components of the high-latitude ionospheric plasma dynamics. Considering the close relation between SAPS and FACs, it is thus intriguing to study small- or meso-scale SAPS variation and the corresponding formation mechanism. In this study, temporal evolution of a SAPS event is investigated using multi-instrument observations from VAP, Super Dual Auroral Radar Network (SuperDARN), Geostationary Operational Environmental Satellite (GOES) and SuperMAG. A meso-scale enhancement of SAPS (MS-SAPS+) extending less than 500 km east-west was observed before a substorm onset. Particle injection, local magnetic field dip in the equatorial magnetosphere are observed simultaneously with the SAPS electric field. The MS-SAPS+ occurred near the nightside Harang reversal and all phenomena observed by the above mentioned instruments can be explained due to non-substorm particle injection and the associated localized pressure enhancement in the equatorial magnetosphere. This paper is organized as follows. Section 2 presents the SAPS event observations from both in-situ and ground-based observations. In section 3, the formation mechanism of the mesoscale enhancement of SAPS is discussed and a summary is provided in section 4.

2 Observations

The VAP mission consists of two identically instrumented spacecraft (VAP-A and VAP-B) in nearly identical ~ 9 h orbits, with perigee of ~ 600 km altitude, apogee of $5.8 R_E$, and inclination of 10° (Mauk et al., 2014). With the Electric Field and Waves experiment (EFW) (Wygant et al., 2014) onboard, VAP is an ideal tool to observe the SAPS electric field in the inner magnetosphere. The SAPS event targeted by this paper was observed by VAP-A on May 18, 2013, as shown in Figure 1. The solar wind and interplanetary magnetic field (IMF) conditions during this event are obtained from the NASA OMNI database and shown in Figure 1a. The IMF B_z was continuously southward except a short excursion to northward between 0445UT and 0500 UT. This southward IMF led to a moderate geomagnetic storm with the minimum SYM-H reaching -66 nT. This SAPS event occurred during the recovery phase of the storm (the shaded blue area), when the IMF B_z turned back to northward briefly and then southward again.

Figure 1b presents the DC electric field observed by the EFW instrument in the modified GSE coordinate (MGSE), which is similar to the GSE coordinates. On the duskside, the E_y component in the MGSE coordinates is pointing approximately duskward (Wygant et al., 2014). Since VAP-A was on the duskside, we can recognize E_y approximately as the radial electric field. A clear electric field enhancement pointing radially outward can be seen with its peak exceeding 8 mV/m at $L=3.5$ and $MLT=19.8$ at 0457 UT (indicated by the blue dashed line). This SAPS electric field observation lasted for only 2 min. It is difficult to identify whether this is a spatial or temporal effect based on a single satellite observation. It can be either a small spatial scale structure or a short-lived one. Another possibility is that the spacecraft crossed the edge of the SAPS region and only captured a fraction of it. Figure 1c shows the magnetic field from the Electric and Magnetic Field Instrument Suite and Integrated Science (EMFISIS) fluxgate magnetometer (Kletzing et al., 2014). A local magnetic dip in the GSM B_x and B_z components was encountered by VAP-A at the same time of the SAPS. The electron density derived from the spacecraft potential is shown in Figure 1d. As one can see, SAPS was located slightly earthward of the plasmopause, where the cold electron density suddenly decreased at 0459 UT.

The high energy (50 keV-1 MeV) spin-averaged ion and electron differential fluxes, shown in Figures 1e and 1f respectively, are from the Magnetic Electron Ion Spectrometer (MagEIS) instrument (Blake et al., 2014). A clear dispersionless ion injection (50-200 keV) and an electron flux decrease were observed at about the same time of SAPS. Note that there were jags between different energy channels in the ion flux. However, the amplitude of the jags was small and well within the measurement uncertainty of MagEIS. Figure 1g and 1h present the differential flux of proton and electron from 1 eV to 50 keV

175 from Helium Oxygen Proton Electron mass spectrometer (HOPE) (Funsten et al., 2014).
176 SAPS electric field was located between the inner boundaries of the ion and electron plasma
177 sheets, which means SAPS was located in an ionospheric region with low electron pre-
178 cipitation rate. This low electron precipitation rate may lead to low conductivity in the
179 ionosphere, and is a preferred condition to facilitate the SAPS development according
180 to the current generator theory. The perpendicular ion pressure in Figure 1i and 1j were
181 calculated from HOPE and MagEIS, respectively. The pressure from HOPE was calcu-
182 lated using the ion perpendicular temperature and density, while the pressure from MagEIS
183 was calculated using the differential energy flux. Here for simplicity, we assume that the
184 pitch angle distribution of particles observed by MagEIS is isotropic. Zhao et al. (2015)
185 show that the isotropic assumption would not significantly influence the magnitude of
186 the pressure. In addition, the gradient of pressure rather the absolute value is more im-
187 portant in the FAC generation theory. At this time, the contribution of electrons to the
188 plasma pressure was much smaller than that of the ions and thus ignored. As one can
189 see, the SAPS electric field was located in the region of large ion pressure gradient. Ac-
190 cording to the Vasyliunas equation, this pressure gradient, together with the gradient
191 of flux tube volume, gave rise to the Region-2 downward FACs on the dusk side (Vasyli-
192 unas, 1970), where the conductivity was low due to low electron precipitation shown in
193 Figure 1h. All of these observations are consistent with the current generator theory. Note
194 that the electron plasma sheet boundary shown in Figure 1h is dispersive, which is not
195 expected according to the short circuiting theory (Mishin, 2013).

196 Since observations from one satellite cannot reveal the spatial and temporal vari-
197 ation of the SAPS, it is of vital importance to include the line-of-sight (los) velocity map
198 from SuperDARN in this study. Fortunately, in this event, the footprint of VAP-A was
199 mapped to the west coast of North America, which is well covered by multiple Super-
200 DARN radars. In this study, the los velocity observations from the Christmas Valley West
201 (CVW), Christmas Valley East (CVE), Blackstone (BKS) and Wallops Island (WAL)
202 SuperDARN radars between 4 UT and 6 UT are considered. Eight selected snapshots
203 of los convection flows are shown in Figures 2-3 and a movie of the whole 2-hour period
204 is provided as supporting information. In Figures 2-3, the color represents the direction
205 and magnitude of the los velocities with blue representing flows towards the radar and
206 red representing flows away from the radar. Three selected beams, CVW beam 14, CVE
207 beam 0 and 9 are indicated by black dashed lines in the panel of 0448 UT, which will
208 be discussed later. The equatorward boundary of the auroral oval, indicated by the yel-
209 low dashed line in Figures 2-3 is based on the auroral observations centered at 0425 UT
210 and from the Special Sensor Ultraviolet Spectrographic Imager (SSUSI) instrument on-
211 board the Defense Meteorological Satellite Program (DMSP) F18. The VAP-A VAP-B
212 and GOES-15 are mapped to the ionosphere based on the Tsyganenko Geomagnetic Field
213 (TS05) model (Tsyganenko & Sitnov, 2005) and are shown as purple (VAP-A and B)
214 and green (GOES15) stars in Figures 2-3, respectively. Seven ground-based magnetome-
215 ters close to the west coast are shown as blue crosses. Two orbital planes of the Iridium
216 satellite near the west coast are also indicated as red lines. As one can see, the footprint
217 of VAP-A was located just equatorward of the DMSP SSUSI auroral equatorward bound-
218 ary, which is consistent with the VAP-A observations shown in Figure 1 that the SAPS
219 electric field was earthward of the electron plasma sheet boundary.

220 As shown in Figure 2, at 0420 UT, in the early recovery phase of the storm, a large-
221 scale SAPS (LS-SAPS) had fully developed and extended across the whole North Amer-
222 ica continent with peak flow speed exceeding 1000 m/s. At 0446 UT, when the IMF turned
223 northward, due to the weakening of the convection, the amplitude of the LS-SAPS de-
224 creased to ~ 400 m/s. Another feature is that an equatorward flow, highlighted by a black
225 arrow, occurred poleward of the LS-SAPS and near the footprint of GOES 15 with peak
226 flow amplitude of ~ 400 m/s. It continued to propagate equatorward at 0448 UT. At 0450
227 UT, the westward flow near the end of the equatorward flow and near the C13 magne-
228 tometer suddenly enhanced to ~ 600 m/s, while the equatorward flow at higher latitudes

229 disappeared. This SAPS flow enhancement was localized and extended less than 10 de-
230 grees in longitude. The eastern part of the LS-SAPS changed little.

231 In Figure 3, at 0456 UT, another equatorward flow developed near a cluster of mag-
232 netometers and again highlighted by a black arrow. At 0458 UT, the equatorward flow
233 moved westward to near the footprint of GOES 15 and sustained the enhancement of
234 westward flow. A very rough estimation of the westward movement of the equatorward
235 flow is $2.5^\circ/min$, corresponding an azimuthal velocity of 30 km/s in the GEO orbit. This
236 velocity is comparable with the magnetic drift speed of a 50 keV proton, and is consis-
237 tent with the energy range of the particle injection observed by VAP-A. At 0500 UT,
238 both the equatorward and westward flows began to decrease and at 0504 UT the flow
239 returned back to the background value. Note that the large westward flow near the mag-
240 netometers SIT and T22 are 1-1/2 hop scatter, an artificial signal due to the ground scat-
241 tering. Combining the VAP-A and SuperDARN observations, it is highly likely that VAP-
242 A passed the western edge of this SAPS enhancement region. Considering the spatial
243 scale of this SAPS enhancement is much smaller than the large-scale background SAPS,
244 which extends over several hours of MLT, this SAPS enhancement is thus called a meso-
245 scale enhancement of SAPS (MS-SAPS+).

246 The los velocity from CVW beam 14, CVE beam 9 and CVE beam 0 are presented
247 in Figures 4 and 5. The looking direction of these three beams are indicated by black
248 dashed lines in Figure 2. The CVW beam 14 and CVE beam 9 together are used to con-
249 firm the localization of this SAPS enhancement. Figure 4a shows the los velocity mea-
250 sured by the CVW beam 14 as a function of magnetic latitude and universal time, which
251 is looking westward. The red color indicates that the flows were moving away from the
252 radar, corresponding to westward flows. As one can see, the westward flow was weak be-
253 fore 0450 UT. There were two sudden enhancements at 0450 and 0455 UT respectively,
254 indicated by green squares, consistent with the two SAPS enhancements following the
255 equatorward flow bursts. Figure 4b is in the same format as Figure 4a but for CVE beam
256 9, which is looking eastward, and the blue color represents the flow were towards the radar,
257 thus also corresponding to westward flows. The westward flow observed by the CVE beam
258 9 did not show any enhancement between 0450-0500 UT. Therefore, the comparison be-
259 tween the two beams looking at different sections of the LS-SAPS demonstrated that the
260 enhancement of SAPS was localized. Los observations from the CVE beam 0 and the
261 keogram from all sky imager (ASI) at Saskatoon are shown in Figure 5. The keogram
262 is taken at $50^\circ W$ and check the movie of the ASI measurements in the supporting ma-
263 terial. As shown in Figure 2, beam 0 is looking approximately poleward. The blue color
264 represents that the flows are moving mainly towards the radar, corresponding to equa-
265 torward flows. The field of view of the ASI is also shown in Figure 2. One can see that
266 the CVE Beam 0 is near the western edge of the ASI and it observed both equatorward
267 flow enhancements at 0446 and 0456 UT, respectively. The timing is consistent with that
268 of the westward enhancements at lower latitude in Figure 4a. Although it was cloudy,
269 it still can be seen from the keogram that the aurora activity increased simultaneously
270 with the first flow burst. However, no aurora activity was observed within the Saskatoon
271 ASI during the second flow burst. This is very likely because the flow burst was observed
272 by SuperDARN further to the west and away from the ASI and thus the corresponding
273 aurora activity is out of the scope of the ASI.

274 The orbital plane of AMPERE near 20 MLT is also presented in Figure 4a and the
275 black arrows represent the vectors of the magnetic perturbations observed by AMPERE.
276 The vector along the x (y) axis represents the perturbation in the west-east (north-south)
277 direction. The perturbation in the vertical direction is not reflected in Figure 4a. It is
278 shown that when the MS-SAPS+ developed, the magnetic perturbations and the down-
279 ward FAC were both enhanced. The peak of the downward FAC, where the perturba-
280 tion changed its direction, is denoted by the black circle. Note that the enhancement later
281 at 0510 UT was related with a substorm onset observed by ground-based ASI (not shown).

282 During this event, VAP-B, GOES 13 and 15 were also located in the dusk-midnight
 283 sector, which can provide large-scale picture about the particle injection activities. Their
 284 orbits from 0415 UT to 0515 UT are shown in Figure 6a. Both VAP-A and GOES-15
 285 were at ~ 20 MLT, while VAP-B was at ~ 22 MLT and GOES 13 was right around mid-
 286 night. The proton and electron fluxes observed by GOES 15 are shown in Figure 6b and
 287 6c and the magnetic field in GSM coordinate is shown in Figure 6d. Three injections were
 288 observed at 0444 UT, 0450 UT and 0506 UT respectively and are indicated by gray ar-
 289 rows. The timing of the first injection is consistent with the first equatorward flow burst
 290 at 0446 UT observed by SuperDARN in Figure 2b. Considering the footprint of GOES
 291 15 was very close to the flow channel, both the injection and its manifestation in the iono-
 292 sphere were thus observed simultaneously. The second injection is likely associated with
 293 the SAPS event observed by VAP-A. Considering the conservation of the first adiabatic
 294 invariant, the ions of 200 keV energy observed by VAP-A at $L=3.5$ should have an ini-
 295 tial energy around 30 keV at the geosynchronous orbit. Although this energy is lower
 296 than the lowest energy of GOES, i.e., 95 keV, we can use the arrival time of 95 keV ion
 297 to roughly estimate the arrival time of 30 keV in the case of dispersionless injection. Both
 298 VAP-B and GOES 13 were on the night side during this event, but they did not observe
 299 any injections. This suggests that the injection was localized and likely from the dusk
 300 side rather than from the night side. The radial injection speed is estimated to be ~ 47
 301 km/s. The velocity is estimated using the positions of two spacecraft and the time dif-
 302 ference between the flux increase observed by these two spacecraft. This calculated in-
 303 jection velocity is reasonable (Moore, Arnoldy, Feynman, & Hardy, 1981; Reeves et al.,
 304 1996) and suggests that the injections observed by VAP-A and GOES 15 are possibly
 305 the same one. The third injection was associated with a substorm onset at 0510 UT ob-
 306 served by ground-based ASI and was later than the SAPS event observed by VAP-A.

307 No magnetic field dipolarization was observed by GOES-15 accompanying the first
 308 injection (Figure 6d). After the injection observed by GOES-15, energetic electrons will
 309 move eastward due to gradient and curvature drift, thus it is not likely to be observed
 310 by VAP-A that was westward of GOES 15. The second and the third injections were both
 311 accompanied by a magnetic dipolarization. This infer that the first injection did not have
 312 enough energy to significantly disturb the ambient geomagnetic field at the geosynchronous
 313 orbit.

314 Seven ground magnetometer data obtained from SuperMAG (Gjerloev, 2012) were
 315 used to study the magnetic perturbation associated with the SAPS and auroral activ-
 316 ities. Daily average was subtracted from the raw data. Their locations relative to the
 317 SAPS and auroral boundary are also shown in Figure 2. Negative bays were observed
 318 by C12, T36, C06, RED at 0450 UT. This time is consistent with the time of the MS-
 319 SAPS+ (Figure 2). Stations that observed negative bays all located on the east side of
 320 the MS-SAPS+. At the same time, positive bays were observed by C13, T22 and SIT,
 321 which are close to the MS-SAPS+. Negative (positive) bays are due to enhancement of
 322 westward (eastward) auroral currents and thus eastward (westward) convection flows.
 323 These observations suggest an overlapping of the westward and eastward currents and
 324 flows over a narrow latitudinal region comprises the Harang reversal, which can be nicely
 325 explained by the schematic plot shown in Figure 8, adapted from Figure 14a in Zou, Lyons,
 326 Nicolls, et al. (2009).

327 In Figure 8, the black curved line represents the equipotential line near the Harang
 328 reversal region. VAP-A (magenta star) observed the radially outward electric field and
 329 its footprint is located in the equatorward portion of the Harang reversal. The beams
 330 of CVW looking westward observed westward flows. C13, T22 and SIT observed posi-
 331 tive magnetic perturbations, due to eastward auroral electrojet and westward convec-
 332 tion flows. On the other hand, at the poleward portion of the Harang reversal, negative
 333 magnetic perturbations were observed by C12, T36, C06, RED and equatorward flows
 334 were observed by beams looking poleward.

3 Discussion

The SAPS electric field and other complementary measurements from VAP-A presented in Figure 1 are consistent with the current generator theory. At first, when the injected particles traveled towards the inner magnetosphere, they were adiabatically energized in order to conserve the first adiabatic invariant. At the geosynchronous orbit, they may not have enough energy to depress the magnetic field. As they moved closer to the plasmapause, these particles were energized enough and could depress the magnetic field according to the diamagnetic effect (Gurgiolo, Lin, Mauk, Parks, & McIlwain, 1979; Z. He et al., 2017; Xia, Chen, Zheng, & Chan, 2017; Xiong et al., 2017). The magnetic dip in the inner magnetosphere is important for both the generation of butterfly pitch angle distributions (PADs) of electrons (Xiong et al., 2017) and electromagnetic ion cyclotron (EMIC) wave (Z. He et al., 2017; Remya et al., n.d.). The magnetic field dip led to the decreasing of the energetic electron flux (Figure 1e) due to conservation of the first adiabatic invariant of electrons, consistent with earlier observations (Z. He et al., 2017). In this case, butterfly PADs were also observed by VAP-A at the energy of 31 keV (not shown).

We further tested the diamagnetic properties in the SAPS region. We first used the TS05 magnetic field magnitude minus 48 nT to fit the general trend of magnetic field ignoring the magnetic dip. Then this magnetic field was compared with the observed magnetic field, which shows that the magnetic pressure decreased by ~ 17 nPa at the center of magnetic dip and SAPS peak. The increase of the ion plasma pressure was about 12 nPa with contributions from both HOPE and MagEIS ($\Delta P_{HOPE} + \Delta P_{MagEIS} = 7 + 5$ nPa). This was quantitatively similar to the magnetic pressure decrease. Therefore, the magnetic field dip can be explained by the particle injections and the diamagnetic effects. This also shows that the injected particles can make a large contribution to the storm time ring current, as shown in (Gkioulidou et al., 2014). Another interesting point is that this injection was observed to enter the inner magnetosphere at ~ 20 MLT and no injection was observed closer to the midnight sector. Therefore, this injection might be related with dynamics near the magnetopause flank, such as Kelvin-Helmholtz instability (Henderson, 2013). However, the exact source of the particle injection is out of the scope of this paper.

When a plasma pressure peak was generated in the inner magnetosphere, together with the gradient of the flux tube volume, a pair of Region-2 sense FACs can be generated near the edges of this dip (Figure 9), according to the Vasyliunas equation. In addition, this region was between the inner boundaries of ion and electron plasma sheets, and thus the region where the downward FAC flows into in the ionosphere was of low conductivity. When the downward FAC closed poleward through the Pederson current and the upward Region-1 sense FAC, the electric field needed to increase to maintain current continuity. The above scenario explains the large poleward electric field in the ionosphere and radially outward electric field in the magnetosphere.

The results above lead to the schematic diagram of the formation of SAPS given in Figure 9. During geomagnetic storm time, a partial ring current develops due to the enhanced convection. The gradient of plasma thermal pressure in partial ring current and the gradient of the flux tube volume can generate the Region-2 FACs and thus SAPS (Anderson et al., 1993; Southwood & Wolf, 1978). This large-scale SAPS should have a spatial scale comparable with the partial ring current and can extend several hours of MLT. However, when a localized injection entering the inner magnetosphere and merging into the pre-existing partial ring current, a localized pressure peak should form. At the same time, due to the diamagnetic effect, a local magnetic field dip can develop at the same location. The gradient of the flux tube volume points towards the local magnetic minimum. Therefore, the perturbed plasma pressure gradient and the flux tube volume gradient give rise to two pairs of FACs. The duskside pair is the Region-2 sense downward FACs close to the Earth and Region-1 sense upward FACs further away from the

388 Earth. The other pair closer to midnight would have opposite polarity. These two pairs
389 of FACs thus comprise a two-loop current wedge (2LCW). In duskside ionosphere, the
390 Region-2 sense FACs close through poleward Pederson current and then upward Region-
391 1 sense FACs. This Pederson current flows in a low-conductivity region equatorward of
392 the electron precipitation boundary and thus leads to a large poleward electric field, i.e.,
393 SAPS electric field. Meanwhile, these FACs pairs superpose on top of the large-scale FAC
394 systems near the equatorward edge of the aurora oval. This 2LCW can also explain the
395 magnetic dip in the MGSE x direction. At the dusk side, the MGSE Bx component can
396 be considered westward. Both the downward FAC earthward of the dip and upward FAC
397 further away from the dip can generate an eastward magnetic disturbance and thus re-
398 duce the Bx component in the MGSE coordinates. Note that this 2LCW should be dif-
399 ferentiated against the 2L substorm current wedge (SCW). The latter is formed after sub-
400 storm onset although the formed FACs have similar polarities. In addition, no local mag-
401 netic field dip is invoked in the 2L SCW scenario. This mechanism can also be applied
402 to LS-SAPS: The spatial scale of the SAPS depends on the scale of the particle injec-
403 tion. Injections can have variable scales from less than 1 hour in MLT, e.g. in this event,
404 to three hours in MLT in substorm injections, to the whole night side during sawtooth-
405 type injections (Arnoldy & Moore, 1983; Clauer, Cai, Welling, DeJong, & Henderson,
406 2006; McPherron, 2015). Thus, the scale-size of the SAPS enhancement should be di-
407 rectly related with the scale-size of injections.

408 Auroral streamers in the ionosphere have been proposed to be the corresponding
409 signature of flow bursts in the equatorial magnetosphere or injections when flow bursts
410 reach the geosynchronous orbit (Forsyth et al., 2008; Henderson, Reeves, & Murphree,
411 1998; Nakamura et al., 2001; Sergeev et al., 1999; Zou, Lyons, Wang, et al., 2009). Gallardo-
412 Lacourt et al. (2017) showed that 98% streamers reaching equatorward boundary of the
413 auroral oval are associated with SAPS and there is a strong correlation between the du-
414 ration of SAPS and streamers. Nishimura et al. (2011) showed that not all streamers can
415 lead to substorm onset. Thus, it is reasonable to infer that substorm onset is not nec-
416 essary for streamers or particle injections, and thus SAPS. Enhanced auroral activity was
417 indeed observed during the first equatorward flow and SAPS enhancement, but it was
418 not observed during the second case. This is very likely because the flow burst was ob-
419 served by SuperDARN beams looking west of the ASI, and thus the corresponding au-
420 rora activity is out of the field-of-view of the ASI.

421 Dispersionless particle injections are often observed during substorms right at or
422 slightly after the substorm onset and have been used as a reliable substorm onset indi-
423 cator. However, injections and substorms do not have a one-to-one correspondence (e.g.
424 Angelopoulos et al., 1992; Gkioulidou et al., 2014). Sergeev et al. (1990) showed that in-
425 jections can occur during steady convection time in addition to substorm time. This also
426 suggests that substorm onset may not be necessary for injections and thus the forma-
427 tion of SAPS. Instead, SAPS can be generated directly by particle injections.

428 **4 Summary and Conclusions**

429 In this study, we performed a detailed case study of SAPS during the storm recov-
430 ery phase on May 18, 2013 using conjugate VAP and SuperDARN as well as other com-
431plementary instruments. Energetic ion injections, energetic electron flux decrease, and
432 local magnetic field dip were observed at the same time as the SAPS electric field by VAP-
433 A deep in the inner magnetosphere at 3.5 Re. The formation mechanism of the SAPS
434 is suggested to be due to energetic particle injection together with the magnetic field dis-
435 tortion due to the injected particles' diamagnetic effect, which can generate a localized
436 2LCW with SAPS on its western side. SAPS is also shown to be part of the equator-
437 ward boundary of the Harang reversal, which started to develop before the substorm on-
438 set. Considering the correspondence between substorms and injections is not one-to-one,
439 we suggest that SAPS can be generated directly due to particle injections induced pres-

440 sure and flux tube volume gradients, no matter whether these injections are directly related
441 with a substorm onset or not.

442 Acknowledgments

443 We acknowledge NSF AGS1342968 and NASA NNX14AF31G for supporting the work
444 at the University of Michigan. Processing and analysis of the HOPE and MagEIS data
445 was supported by Energetic Particle, Composition, and Thermal Plasma (RBSP-ECT)
446 investigation funded under NASA Prime contract no. NAS5-01072. All RBSP-ECT data
447 are publicly available at the Web site <http://www.RBSP-ect.lanl.gov/>. We acknowl-
448 edge the Van Allen Probe EMFISIS and EFW teams for data usage. The EMFISIS and
449 EFW data used in the study are obtained from <http://emfisis.physics.uiowa.edu/>,
450 <http://www.space.umn.edu/rbspefw-data/>, respectively. We appreciate the discus-
451 sion with Dr. S. Claudepierre about the MagEIS data. We thank GOES, SuperDARN
452 and SuperMAG team for high quality data. SuperDARN and SuperMAG data are from
453 <https://www.ngdc.noaa.gov/stp/satellite/goes/>, <http://vt.superdarn.org/> and
454 <http://supermag.jhuapl.edu/> respectively. The OMNI data are available at CDAWeb.
455 The aurora image files from ASI at Saskatoon can be found at [https://deepblue.lib](https://deepblue.lib.umich.edu/data/concern/generic_works/hq37vp515?locale=en)
456 [.umich.edu/data/concern/generic_works/hq37vp515?locale=en](https://deepblue.lib.umich.edu/data/concern/generic_works/hq37vp515?locale=en).

457 References

- 458 Anderson, P. C. (2004). Subauroral electric fields and magnetospheric convection
459 during the April, 2002 geomagnetic storms. *Geophysical Research Letters*,
460 *31*(11), 2000–2003. doi: 10.1029/2004GL019588
- 461 Anderson, P. C., Carpenter, D. L., Tsuruda, K., Mukai, T., & Rich, F. J. (2001).
462 Multisatellite observations of rapid subauroral ion drifts (SAID). *Journal of*
463 *Geophysical Research*, *106*(A12), 29585. doi: 10.1029/2001JA000128
- 464 Anderson, P. C., Hanson, W. B., Heelis, R. A., Craven, J. D., Baker, D. N., &
465 Frank, L. A. (1993). A proposed production model of rapid subauroral ion
466 drifts and their relationship to substorm evolution. *Journal of Geophysical*
467 *Research*, *98*(92), 6069. doi: 10.1029/92JA01975
- 468 Anderson, P. C., Heelis, R. A., & Hanson, W. B. (1991). The ionospheric signatures
469 of rapid subauroral ion drifts. *Journal of Geophysical Research*, *96*(90), 5785.
470 doi: 10.1029/90JA02651
- 471 Angelopoulos, V., Baumjohann, W., Kennel, C. F., Coroniti, F. V., Kivelson, M. G.,
472 Pellat, R., . . . Paschmann, G. (1992). Bursty bulk flows in the inner cen-
473 tral plasma sheet. *Journal of Geophysical Research*, *97*(A4), 4027. doi:
474 10.1029/91JA02701
- 475 Arnoldy, R., & Moore, T. (1983). Longitudinal structure of substorm injections
476 at synchronous orbit. *Journal of Geophysical Research: Space Physics*, *88*(A8),
477 6213–6220.
- 478 Banks, P. M., & Yasuhara, F. (1978). Electric fields and conductivity in the night-
479 time E-region. *Geophysical Research Letters*, *5*(12), 1047–1050.
- 480 Blake, J. B., Carranza, P. A., Claudepierre, S. G., Clemmons, J. H., Crain, W. R.,
481 Dotan, Y., . . . Zakrzewski, M. P. (2014). The Magnetic Electron Ion Spec-
482 trometer (MagEIS) instruments aboard the Radiation Belt Storm Probes
483 (RBSP) spacecraft. *The Van Allen Probes mission*, *9781489974*, 383–421. doi:
484 10.1007/978-1-4899-7433-4-12
- 485 Burke, W. J., Rich, F. J., De, O., Beaujardiere, L., Huang, C. Y., & Wilson, G. R.
486 (2000). Ionospheric disturbances observed by DMSP at middle to low lati-
487 tudes during the magnetic storm of June 4-6. *Journal of Geophysical Research*,
488 *105*405(1), 391–18.
- 489 Buzulukova, N., Fok, M.-C., Pulkkinen, A., Kuznetsova, M., Moore, T. E., Glocer,
490 A., . . . Rastaetter, L. (2010). Dynamics of Ring Current and Electric Fields

- 491 in the Inner Magnetosphere During Disturbed Periods: CRCM-BATS-R-US
 492 Coupled Model. *Journal of Geophysical Research : Space Physics*, *115*, 1–19.
 493 doi: 10.1029/2009JA014621
- 494 Califf, S., Li, X., Wolf, R. A., Zhao, H., Jaynes, A. N., Wilder, F. D., ... Redmon,
 495 R. (2016). Large-amplitude electric fields in the inner magnetosphere: Van
 496 Allen Probes observations of subauroral polarization streams. *Journal of*
 497 *Geophysical Research : Space Physics*, 1–3. doi: 10.1002/2016JA023362
- 498 Clauer, C. R., Cai, X., Welling, D., DeJong, A., & Henderson, M. G. (2006). Char-
 499 acterizing the 18 april 2002 storm-time sawtooth events using ground magnetic
 500 data. *Journal of Geophysical Research: Space Physics*, *111*(A4).
- 501 Clausen, L. B. N., Baker, J. B. H., Ruohoniemi, J. M., Greenwald, R. A., Thomas,
 502 E. G., Shepherd, S. G., ... Sazykin, S. (2012). Large-scale observations of a
 503 subauroral polarization stream by midlatitude SuperDARN radars: Instanta-
 504 neous longitudinal velocity variations. *Journal of Geophysical Research: Space*
 505 *Physics*, *117*(5), 1–11. doi: 10.1029/2011JA017232
- 506 De Keyser, J. (1999). Formation and evolution of subauroral ion drifts in the
 507 course of a substorm. *Journal of Geophysical Research : Space Physics*, *104*,
 508 339–349.
- 509 Erickson, P. J., Beroz, F., & Miskin, M. Z. (2011). Statistical characterization of
 510 the American sector subauroral polarization stream using incoherent scatter
 511 radar. *Journal of Geophysical Research: Space Physics*, *116*(3), 1–8. doi:
 512 10.1029/2010JA015738
- 513 Forsyth, C., Lester, M., Cowley, S. W., Dandouras, I., Fazakerley, A. N., Fear, R. C.,
 514 ... Watermann, J. (2008). Observed tail current systems associated with
 515 bursty bulk flows and auroral streamers during a period of multiple substorms.
 516 *Annales Geophysicae*, *26*(1), 167–184. doi: 10.5194/angeo-26-167-2008
- 517 Foster, J. C., & Vo, H. B. (2002). Average characteristics and activity dependence
 518 of the subauroral polarization stream. *Journal of Geophysical Research: Space*
 519 *Physics*, *107*(A12), 1–10. doi: 10.1029/2002JA009409
- 520 Funsten, H. O., Skoug, R. M., Guthrie, A. A., MacDonald, E. A., Baldonado, J. R.,
 521 Harper, R. W., ... Chen, J. (2014). Helium, oxygen, proton, and electron
 522 (HOPE) mass spectrometer for the Radiation Belt Storm Probes mission. *The*
 523 *Van Allen Probes mission*, 423–484. doi: 10.1007/978-1-4899-7433-4-13
- 524 Gallardo-Lacourt, B., Nishimura, Y., Lyons, L., Zou, S., Angelopoulos, V., Donovan,
 525 E., ... Nishitani, N. (2014). Coordinated superdarn themis asi observations of
 526 mesoscale flow bursts associated with auroral streamers. *Journal of Geophysi-*
 527 *cal Research: Space Physics*, *119*(1), 142–150.
- 528 Gallardo-Lacourt, B., Nishimura, Y., Lyons, L. R., Mishin, E. V., Ruohoniemi,
 529 J. M., Donovan, E. F., ... Nishitani, N. (2017). Influence of auroral streamers
 530 on rapid evolution of ionospheric SAPS flows. *Journal of Geophysical Re-*
 531 *search: Space Physics*. Retrieved from [http://doi.wiley.com/10.1002/](http://doi.wiley.com/10.1002/2017JA024198)
 532 [2017JA024198](http://doi.wiley.com/10.1002/2017JA024198) doi: 10.1002/2017JA024198
- 533 Gjerloev, J. W. (2012). The SuperMAG data processing technique. *Journal of Geo-*
 534 *physical Research: Space Physics*, *117*(9), 1–19. doi: 10.1029/2012JA017683
- 535 Gkioulidou, M., Ukhorskiy, A. Y., Mitchell, D. G., Sotirelis, T., Mauk, B. H., &
 536 Lanzerotti, L. J. (2014, sep). The role of small-scale ion injections in the
 537 buildup of Earth's ring current pressure: Van Allen Probes observations of the
 538 17 March 2013 storm. *Journal of Geophysical Research: Space Physics*, *119*(9),
 539 7327–7342. doi: 10.1002/2014JA020096
- 540 Gurgiolo, C., Lin, C. S., Mauk, B., Parks, G. K., & McIlwain, C. (1979). Plasma In-
 541 jection and Diamagnetism. *Journal of Geophysical Research*, *84*(8).
- 542 He, F., Zhang, X.-X., Wang, W., Liu, L., Ren, Z.-P., Yue, X., ... Wang, H. (2018).
 543 Large-scale structure of subauroral polarization streams during the main
 544 phase of a severe geomagnetic storm. *Journal of Geophysical Research: Space*
 545 *Physics*, *123*(4), 2964–2973.

- 546 He, F., Zhang, X.-X., Wang, W., & Wan, W. (2017). Different evolution pat-
 547 terns of subauroral polarization streams (SAPS) during intense storms
 548 and quiet-time substorms. *Geophysical Research Letters*(1998), 1–9. Re-
 549 trieved from <http://doi.wiley.com/10.1002/2017GL075449> doi:
 550 10.1002/2017GL075449
- 551 He, Z., Chen, L., Zhu, H., Xia, Z., Reeves, G. D., Xiong, Y., ... Cao, Y. (2017).
 552 Multiple-Satellite Observation of Magnetic Dip Event During the Sub-
 553 storm on 10 October 2013. *Geophysical Research Letters*, 1–9. doi:
 554 10.1002/2017GL074869
- 555 Heelis, R. A., Bailey, G. J., Sellek, R., Moffett, R. J., & Jenkins, B. (1993). Field-
 556 aligned drifts in subauroral ion drift events. *Journal of Geophysical Research:
 557 Space Physics*, 98(A12), 21493-21499. doi: 10.1029/93JA02209
- 558 Henderson, M. G. (2013). Auroral Substorms, Poleward Boundary Activations,
 559 Auroral Streamers, Omega Bands, and Onset Precursor Activity. *Auroral Phe-
 560 nomenology and Magnetospheric Processes: Earth and Other Planets*, 39–54.
 561 doi: 10.1029/2011GM001165
- 562 Henderson, M. G., Reeves, G. D., & Murphree, J. S. (1998). Are north-south aligned
 563 auroral structures an ionospheric manifestation of bursty bulk flows? *Geophys-
 564 ical Research Letters*, 25(19), 3737. doi: 10.1029/98GL02692
- 565 Huang, C. S., & Foster, J. C. (2007). Correlation of the subauroral polariza-
 566 tion streams (SAPS) with the Dst index during severe magnetic storms.
 567 *Journal of Geophysical Research: Space Physics*, 112(11), 1–8. doi:
 568 10.1029/2007JA012584
- 569 Karlsson, T., Marklund, G. T., Blomberg, L. G., & Mälkki, A. (1998). Subauro-
 570 ral electric fields observed by the Freja satellite: A statistical study. *Journal of
 571 Geophysical Research*, 103(1), 4327. doi: 10.1029/97JA00333
- 572 Kim, K. H., Mozer, F. S., Lee, D. H., & Jin, H. (2010). Large electric field at the
 573 nightside plasmopause observed by the Polar spacecraft. *Journal of Geophys-
 574 ical Research: Space Physics*, 115(7), 2–7. doi: 10.1029/2010JA015439
- 575 Kletzing, C. A., Kurth, W. S., Acuna, M., MacDowall, R. J., Torbert, R. B.,
 576 Averkamp, T., ... Tyler, J. (2014). The Electric and Magnetic Field In-
 577 strument suite and Integrated Science (EMFISIS) on RBSP. *The Van Allen
 578 Probes mission*, 127–181. doi: 10.1007/978-1-4899-7433-4-5
- 579 Kunduri, B. S., Baker, J. B., Ruohoniemi, J. M., Thomas, E. G., Shepherd, S. G., &
 580 Sterne, K. T. (2017). Statistical characterization of the large-scale structure
 581 of the subauroral polarization stream. *Journal of Geophysical Research: Space
 582 Physics*, 122(6), 6035–6048. doi: 10.1002/2017JA024131
- 583 Lejosne, S., & Mozer, F. S. (2017). Sub-Auroral Polarization Stream (SAPS)
 584 duration as determined from Van Allen Probe successive electric drift measure-
 585 ments. *Geophysical Research Letters*. doi: 10.1002/2017GL074985
- 586 Lühr, H., Park, J., Gjerloev, J. W., Rauberg, J., Michaelis, I., Merayo, J. M., &
 587 Brauer, P. (2015). Field-aligned currents' scale analysis performed with the
 588 swarm constellation. *Geophysical Research Letters*, 42(1), 1–8.
- 589 Makarevich, R. A., Kellerman, A. C., Bogdanova, Y. V., & Koustov, A. V. (2009).
 590 Time evolution of the subauroral electric fields: A case study during a se-
 591 quence of two substorms. *Journal of Geophysical Research: Space Physics*,
 592 114(4), 1–13. doi: 10.1029/2008JA013944
- 593 Makarevich, R. A., Kellerman, A. C., Devlin, J. C., Ye, H., Lyons, L. R., &
 594 Nishimura, Y. (2011). SAPS intensification during substorm recovery: A
 595 multi-instrument case study. *Journal of Geophysical Research: Space Physics*,
 596 116(11), 1–16. doi: 10.1029/2011JA016916
- 597 Mauk, B. H., Fox, N. J., Kanekal, S. G., Kessel, R. L., Sibeck, D. G., & Ukhorskiy,
 598 A. (2014). Science objectives and rationale for the Radiation Belt Storm
 599 Probes mission. *The Van Allen Probes mission*, 9781489974, 3–27. doi:
 600 10.1007/978-1-4899-7433-4-2

- 601 McGranaghan, R. M., Mannucci, A. J., & Forsyth, C. (2017). A comprehensive
602 analysis of multiscale field-aligned currents: Characteristics, controlling pa-
603 rameters, and relationships. *Journal of Geophysical Research: Space Physics*,
604 *122*(12).
- 605 McPherron, R. L. (2015). Earth's magnetotail. In *Magnetotails in the solar system*
606 (p. 61-84). American Geophysical Union (AGU). doi: 10.1002/9781118842324
607 .ch4
- 608 Mishin, E. V. (2013). Interaction of substorm injections with the subauroral
609 geospace: 1. Multispacecraft observations of SAID. *Journal of Geophysical*
610 *Research: Space Physics*, *118*(9), 5782–5796. doi: 10.1002/jgra.50548
- 611 Mishin, E. V. (2016). SAPS onset timing during substorms and the westward trav-
612 eling surge. *Geophysical Research Letters*, *43*(13), 6687–6693. doi: 10.1002/
613 2016GL069693
- 614 Mishin, E. V., & Puhl-Quinn, P. A. (2007). SAID: Plasmaspheric short circuit of
615 substorm injections. *Geophysical Research Letters*, *34*(24), 2–5. doi: 10.1029/
616 2007GL031925
- 617 Moore, T., Arnoldy, R., Feynman, J., & Hardy, D. (1981). Propagating substorm in-
618 jection fronts. *Journal of Geophysical Research: Space Physics*, *86*(A8), 6713–
619 6726.
- 620 Nakamura, R., Baurjohann, W., Brittnacher, M., Sergeev, V. A., Kubyshkina, M.,
621 Mukai, T., & Liou, K. (2001). Onset timing and foot point location Brige-
622 Hopfield long filter. *Journal of Geophysical Research*, *106*, 777–789.
- 623 Nishimura, Y., Lyons, L. R., Angelopoulos, V., Kikuchi, T., Zou, S., & Mende, S. B.
624 (2011). Relations between multiple auroral streamers, pre-onset thin arc for-
625 mation, and substorm auroral onset. *Journal of Geophysical Research: Space*
626 *Physics*, *116*(9), 1–10. doi: 10.1029/2011JA016768
- 627 Nishimura, Y., Wygant, J., Ono, T., Iizima, M., Kumamoto, A., Brautigam, D., &
628 Friedel, R. (2008). SAPS measurements around the magnetic equator by CR-
629 RES. *Geophysical Research Letters*, *35*(10), 1–5. doi: 10.1029/2008GL033970
- 630 Oksavik, K., Greenwald, R. A., Ruohoniemi, J. M., Hairston, M. R., Paxton, L. J.,
631 Baker, J. B. H., ... Barnes, R. J. (2006). First observations of the tempo-
632 ral/spatial variation of the sub-auroral polarization stream from the Super-
633 DARN Wallops HF radar. *Geophysical Research Letters*, *33*(12), 1–5. doi:
634 10.1029/2006GL026256
- 635 Puhl-Quinn, P. A., Matsui, H., Mishin, E., Moukikis, C., Kistler, L., Khotyaintsev,
636 Y., ... Lucek, E. (2007). Cluster and DMSP observations of SAID electric
637 fields. *Journal of Geophysical Research: Space Physics*, *112*(5), 1–10. doi:
638 10.1029/2006JA012065
- 639 Reeves, G., Henderson, M., McLachlan, P., Belian, R., Friedel, R., & Korth, A.
640 (1996). Radial propagation of substorm injections. In *International conference*
641 *on substorms* (Vol. 389, p. 579).
- 642 Remya, B., Sibeck, D., Halford, A., Murphy, K., G., Singer, H., ... Thaller, S.
643 (n.d.). Ion injection triggered emic waves in the earth's magnetosphere. *Jour-*
644 *nal of Geophysical Research: Space Physics*.
- 645 Schunk, R. W., Banks, P. M., & Raitt, W. J. (1976). Effects of electric fields and
646 other processes upon the nighttime high-latitude F layer. *Journal of Geophysi-*
647 *cal Research*, *81*(19), 3271. doi: 10.1029/JA081i019p03271
- 648 Sergeev, V. A., Aulamo, O. A., Pellinen, R. J., M., K. V., Bosinger, T., Cattell,
649 C. A., ... Williams, D. J. (1990). NON-SUBSTORM TRANSIENT INJEC-
650 TION EVENTS. *Planetary and Space Science*, *38*(2), 231–239.
- 651 Sergeev, V. A., Liou, K., Meng, C., Newell, P. T., Brittnacher, M., Parks, G., &
652 Reeves, G. D. (1999). Development of auroral streamers in association with
653 localized impulsive injections to the inner magnetotail. *Geophysical Research*
654 *Letters*, *26*(3), 417. doi: 10.1029/1998GL900311
- 655 Southwood, D. J., & Wolf, R. A. (1978). An assessment of the role of precipitation

- 656 in magnetospheric convection. *Journal of Geophysical Research: Space Physics*,
 657 83(A11), 5227–5232. doi: 10.1029/JA083iA11p05227
- 658 Tsyganenko, N. A., & Sitnov, M. I. (2005). Modeling the dynamics of the inner
 659 magnetosphere during strong geomagnetic storms. *Journal of Geophysical Re-*
 660 *search: Space Physics*, 110(A3), 1–16. doi: 10.1029/2004JA010798
- 661 Vasyliunas, V. (1970). *Mathematical Models of Magnetospheric Convection and its*
 662 *Coupling to the Ionosphere* (Vol. 17).
- 663 Wang, H., & Lühr, H. (2011). The efficiency of mechanisms driving Subauroral Po-
 664 larization Streams (SAPS). *Annales Geophysicae*, 29(7), 1277–1286. doi: 10
 665 .5194/angeo-29-1277-2011
- 666 Wang, H., Ridley, A. J., Lühr, H., Liemohn, M. W., & Ma, S. Y. (2008). Statistical
 667 study of the subauroral polarization stream: Its dependence on the cross-polar
 668 cap potential and subauroral conductance. *Journal of Geophysical Research:*
 669 *Space Physics*, 113(12), 1–11. doi: 10.1029/2008JA013529
- 670 Wygant, J. R., Bonnell, J. W., Goetz, K., Ergun, R. E., Mozer, F. S., Bale, S. D.,
 671 ... Tao, J. B. (2014). *The Electric Field and Waves Instruments on the*
 672 *Radiation Belt Storm Probes mission*. doi: 10.1007/978-1-4899-7433-4-6
- 673 Xia, Z., Chen, L., Zheng, L., & Chan, A. A. (2017). Eigenmode analysis of
 674 compressional poloidal modes in a self-consistent magnetic field. *Jour-*
 675 *nal of Geophysical Research: Space Physics*, 122(10), 10,369–10,381. doi:
 676 10.1002/2017JA024376
- 677 Xiong, Y., Chen, L., Xie, L., Fu, S., Xia, Z., & Pu, Z. (2017). Relativistic electron’s
 678 butterfly pitch angle distribution modulated by localized background mag-
 679 netic field perturbation driven by hot ring current ions. *Geophysical Research*
 680 *Letters*, 44(10), 4393–4400. doi: 10.1002/2017GL072558
- 681 Yu, Y., Jordanova, V., Zou, S., Heelis, R., Ruohoniemi, M., & Wygant, J. (2015).
 682 Modeling subauroral polarization streams during the 17 March 2013 storm.
 683 *Journal of Geophysical Research A: Space Physics*, 120(3), 1738–1750. doi:
 684 10.1002/2014JA020371
- 685 Zhao, H., Li, X., Baker, D. N., Fennell, J. F., Blake, J. B., Larsen, B. A., ... Ro-
 686 driguez, J. V. (2015, sep). The evolution of ring current ion energy density
 687 and energy content during geomagnetic storms based on Van Allen Probes
 688 measurements. *Journal of Geophysical Research A: Space Physics*, 120(9),
 689 7493–7511. doi: 10.1002/2015JA021533
- 690 Zou, S., Lyons, L. R., Nicolls, M. J., Heinselman, C. J., & Mende, S. B. (2009).
 691 Nightside ionospheric electrodynamics associated with substorms: PFISR and
 692 THEMIS ASI observations. *Journal of Geophysical Research: Space Physics*,
 693 114(12), 1–24. doi: 10.1029/2009JA014259
- 694 Zou, S., Lyons, L. R., & Nishimura, Y. (2012). Mutual evolution of aurora and iono-
 695 spheric electrodynamic features near the Harang reversal during substorms.
 696 *Geophysical Monograph Series*, 197, 159–169. doi: 10.1029/2011GM001163
- 697 Zou, S., Lyons, L. R., Wang, C. P., Boudouridis, A., Ruohoniemi, J. M., Anderson,
 698 P. C., ... Devlin, J. C. (2009). On the coupling between the Harang reversal
 699 evolution and substorm dynamics: A synthesis of SuperDARN, DMSP, and
 700 IMAGE observations. *Journal of Geophysical Research: Space Physics*, 114(1).
 701 doi: 10.1029/2008JA013449

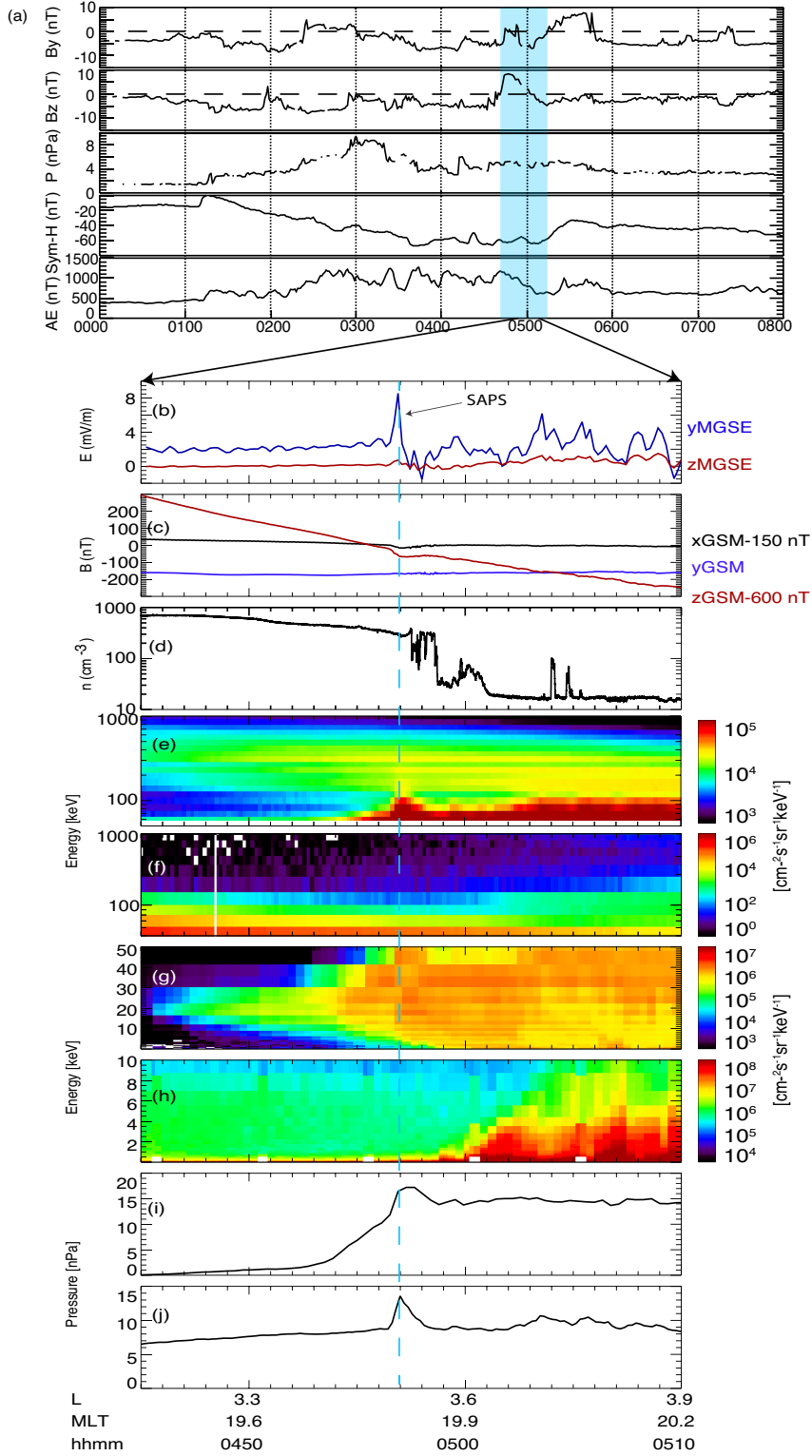


Figure 1. SAPS event on May 18 2013. (a) Solar wind and geomagnetic data from OMNI. (b) Electric field in the MGSE coordinate from EFW. (c) Magnetic field in GSM coordinate from EMFISIS. (d) Electron density from the spacecraft potential. (e) Differential ion flux from MagEIS with energy between 50 keV and 1 MeV. (f) Differential electron flux from MagEIS with energy between 50 keV and 1 MeV. (g) Differential proton flux from HOPE with energy below 50 keV. (h) Differential electron flux from HOPE with energy below 10 keV. (i) Perpendicular ion pressure from HOPE. (j) Perpendicular ion pressure from MagEIS.

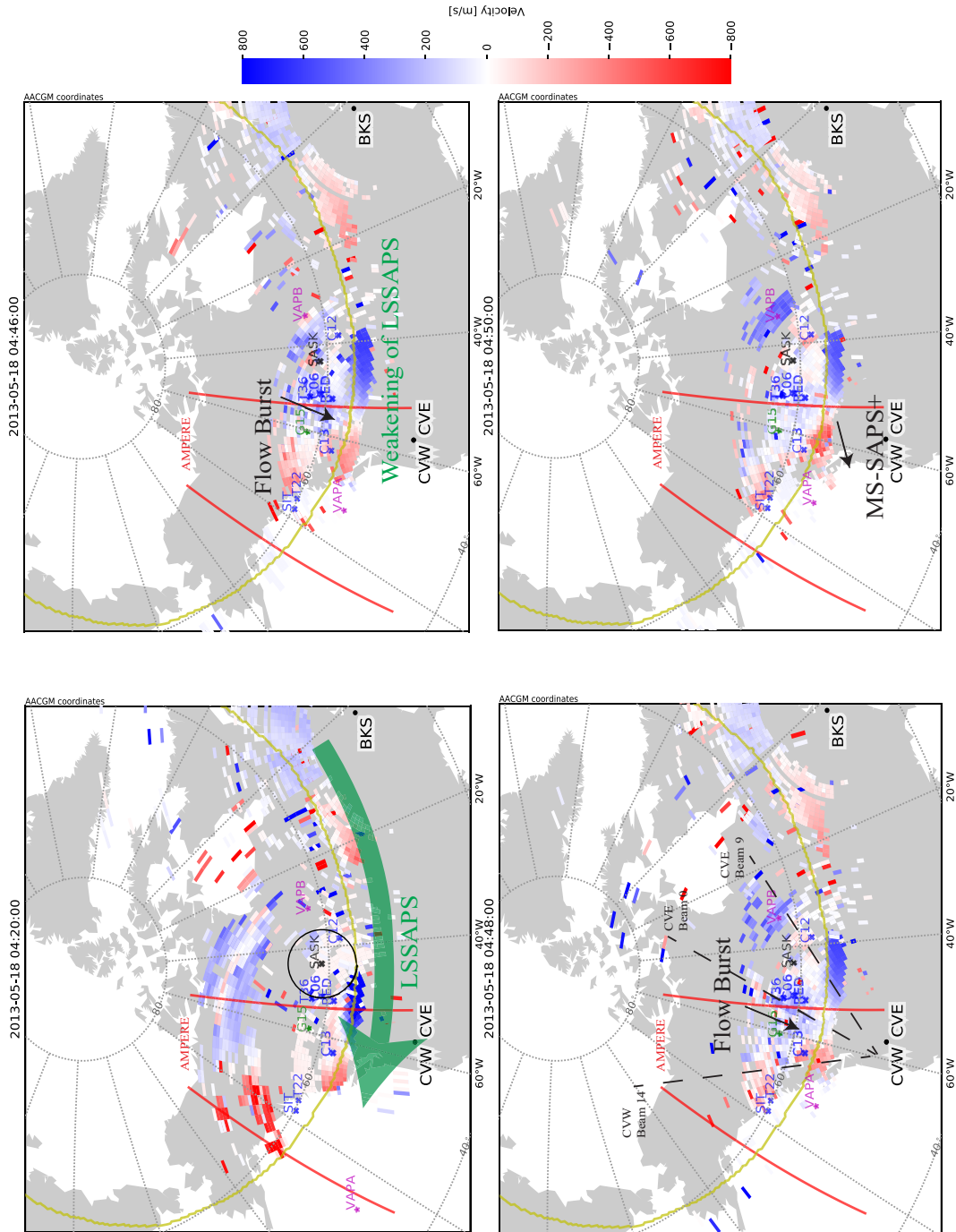


Figure 2. Eight selected maps of the SuperDARN line of sight (los) velocity in the dusk side with ground-based magnetometers, footprints of VAP and GOES, and orbits of AMPERE. Color represents the velocity relative to the radar. Blue means flows are towards the radar and red means flows are away from the radar.

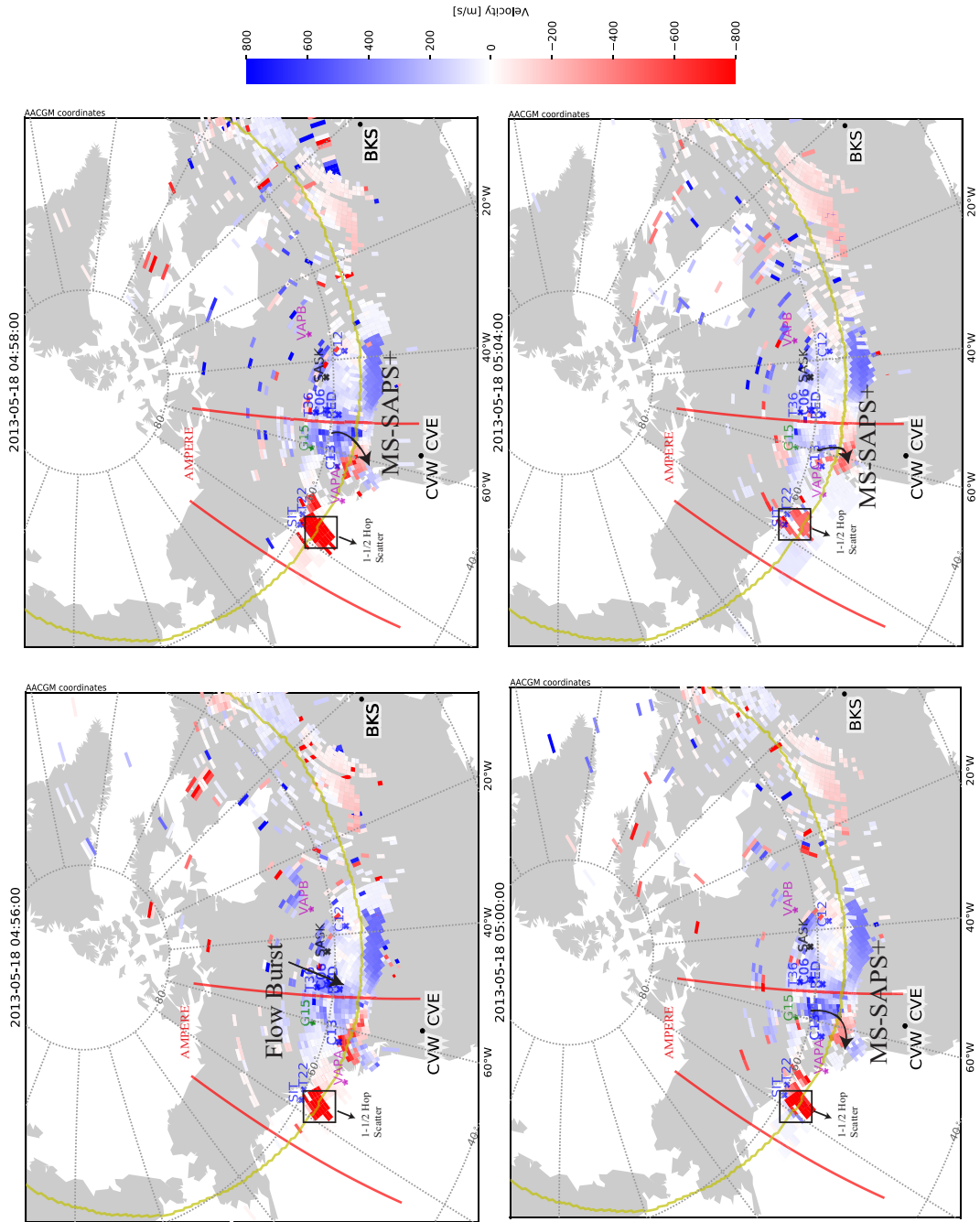


Figure 3. Continued Figure 2.

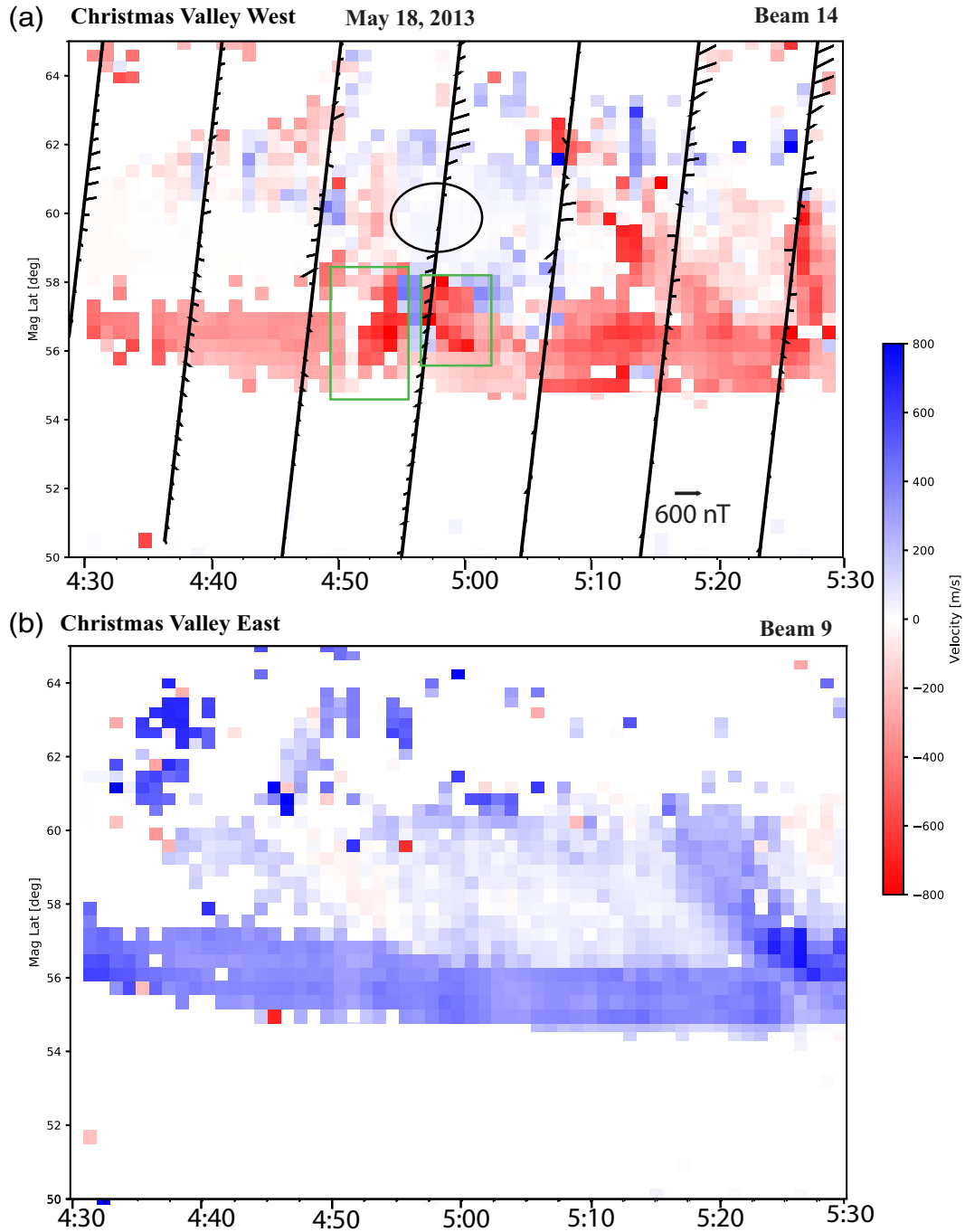


Figure 4. (a) Range-time-intensity (velocity) diagram for the CVW beam 14. The red line represents the AMPERE orbital plane in ~ 20 MLT and the black arrow represents the vector of the magnetic perturbations. (b) Range-time-intensity (velocity) diagram for the CVE beam 9.

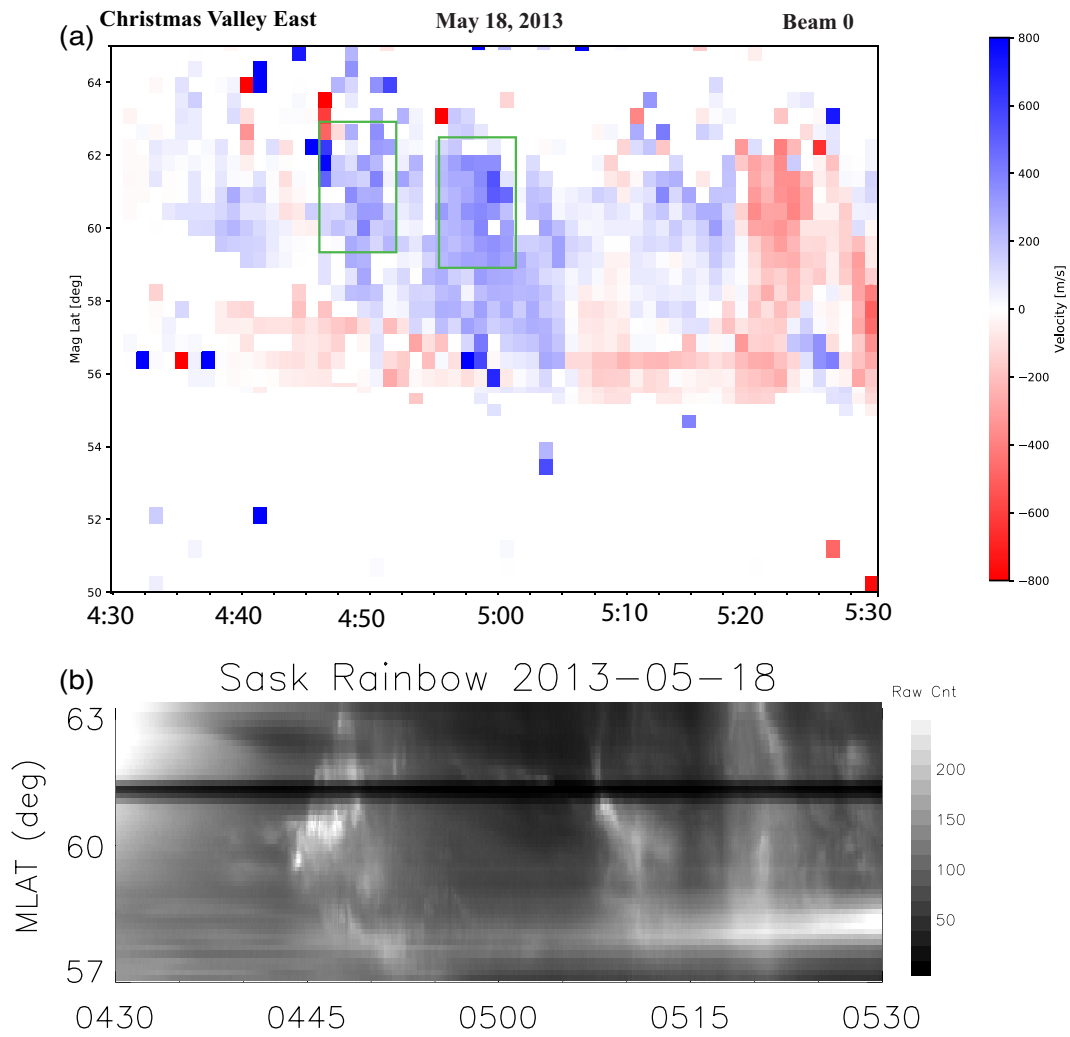


Figure 5. (a) Range-time-intensity (velocity) diagram for the CVE beam 0. (b) Keogram from SASK.

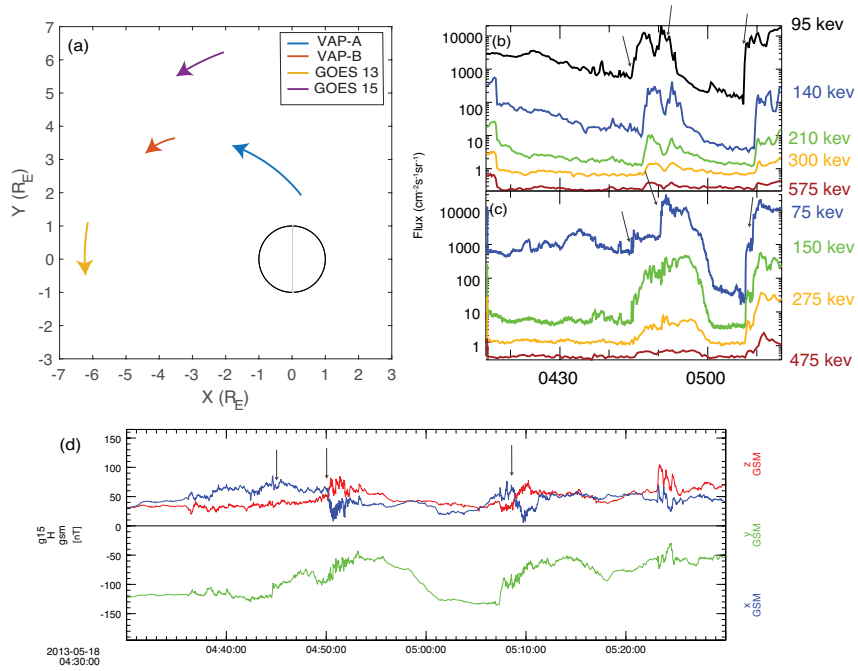


Figure 6. (a) VAP and GOES orbits in the xy plane of GSM coordinate. (b) GOES 15 proton flux. (c) GOES 15 electron flux. (d) GOES magnetic field in GSM coordinate.

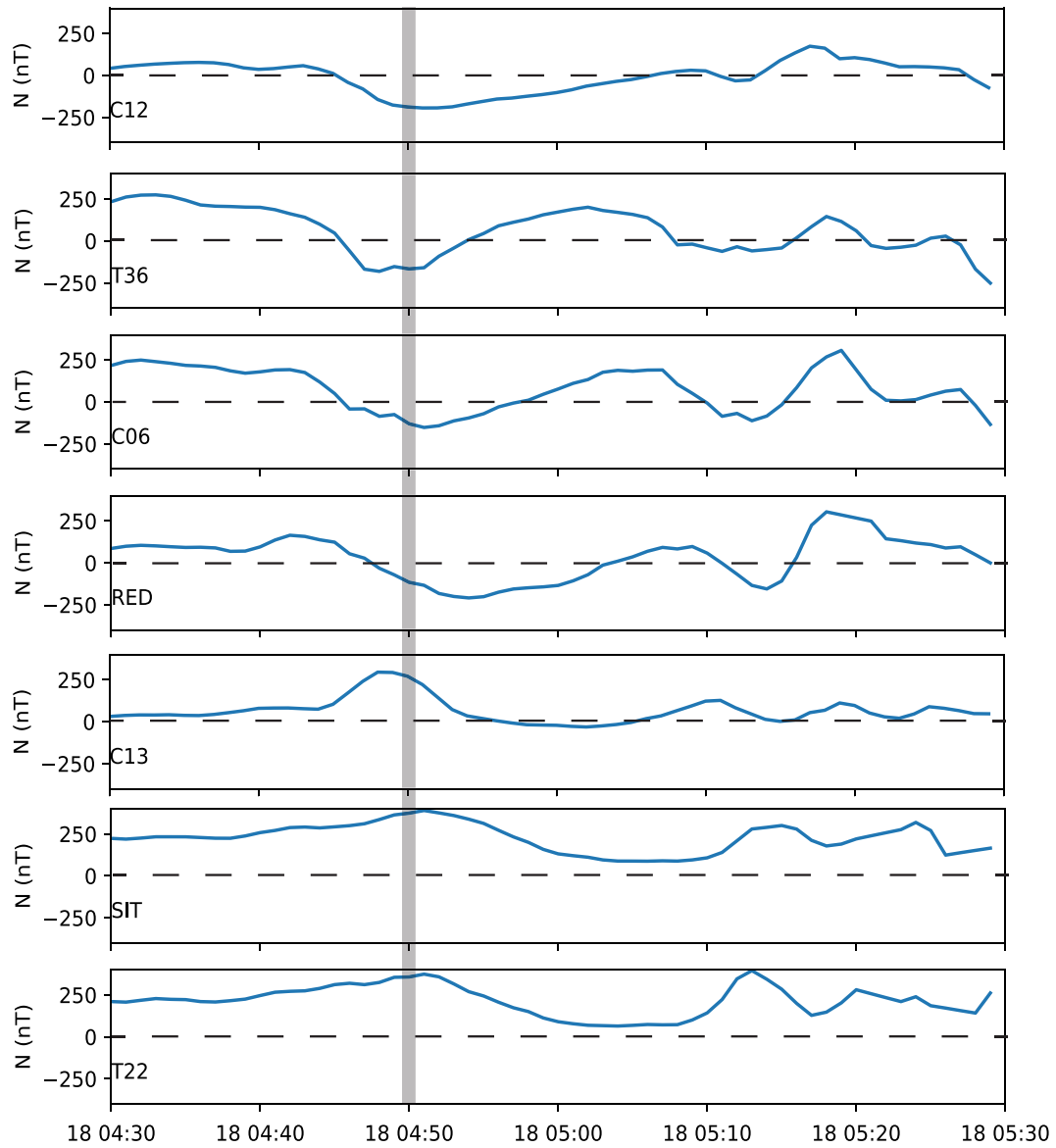


Figure 7. Northward components of the terrestrial magnetic field measured by the ground-based magnetometer stations (taken from SuperMAG).

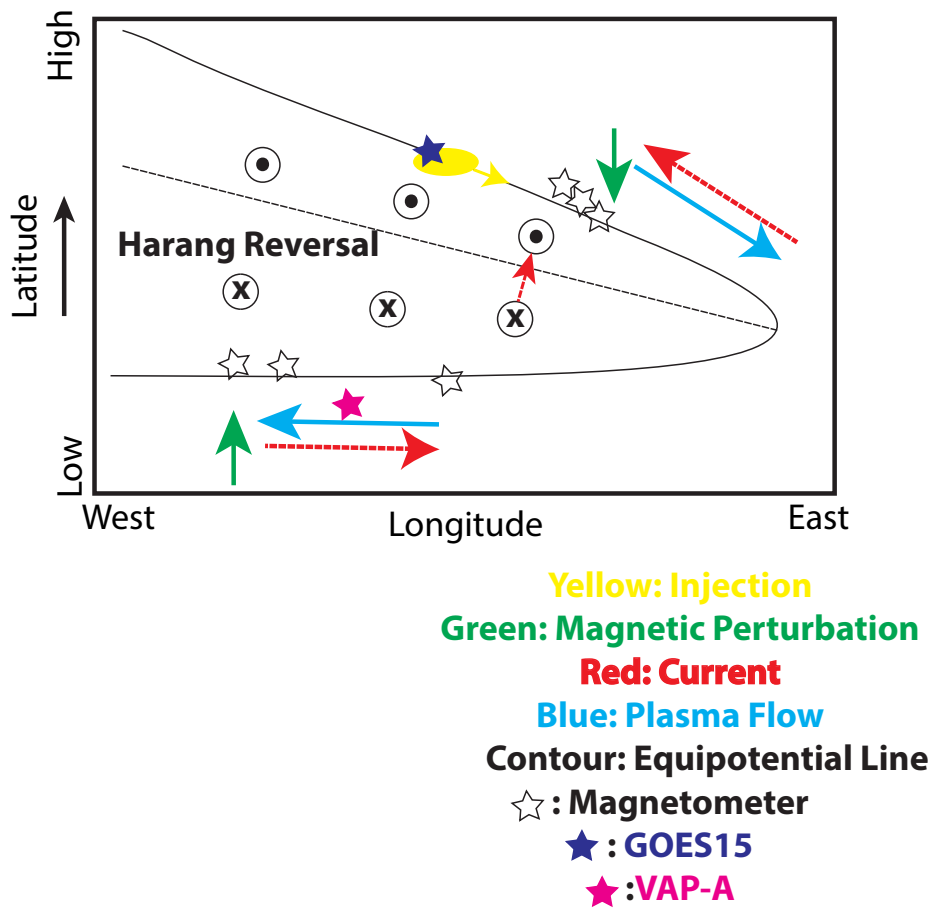


Figure 8. A schematic diagram of the convection flows, field-aligned currents and magnetic perturbations near the Harang reversal.

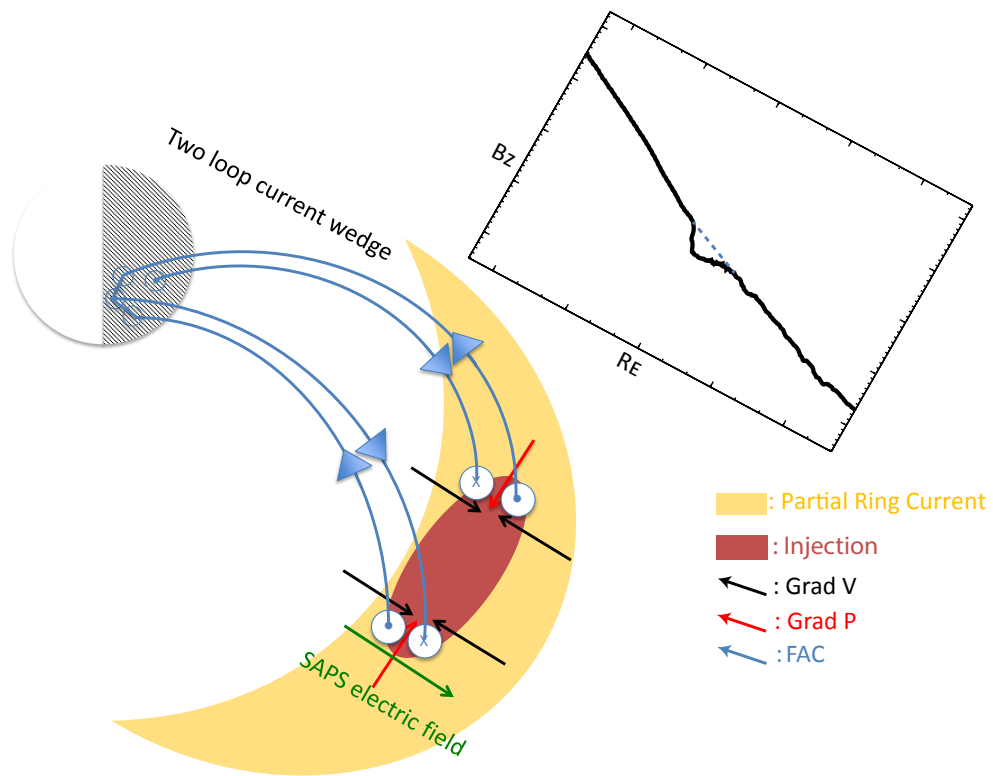


Figure 9. A schematic diagram of the formation of 2LCW and SAPS in the inner magnetosphere.

Figure 1.

Author Manuscript

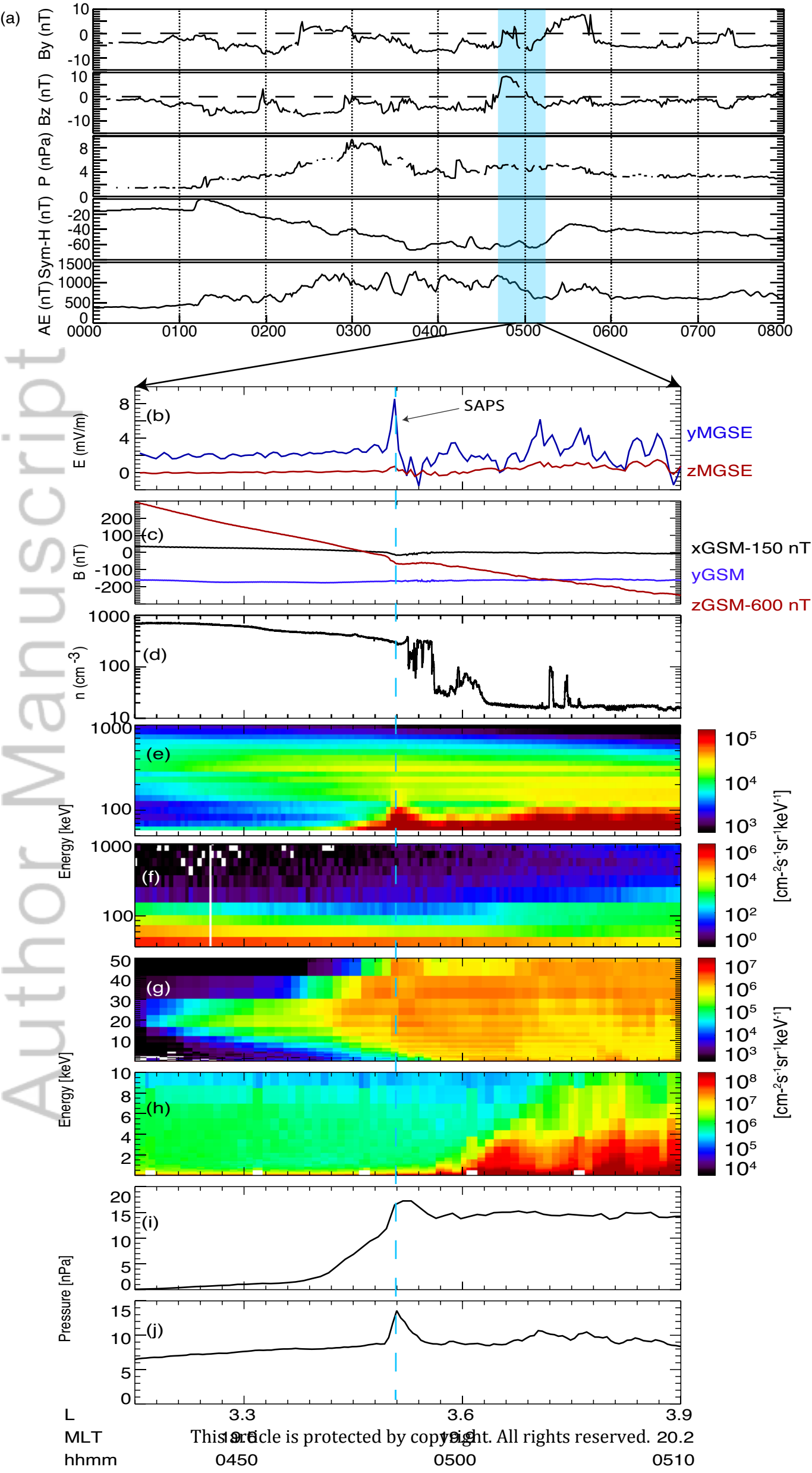
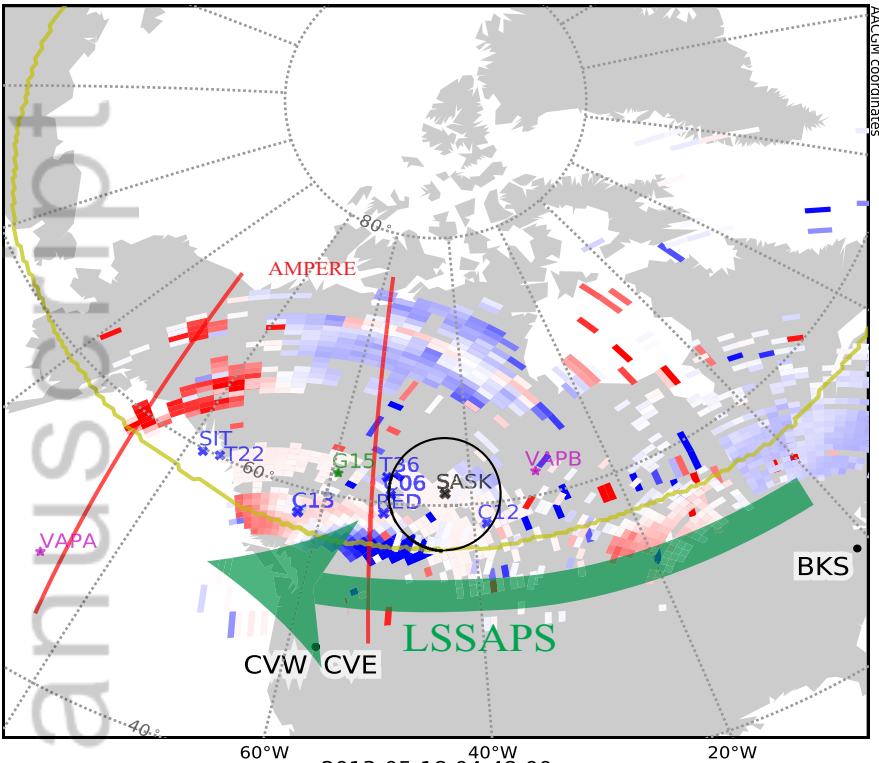


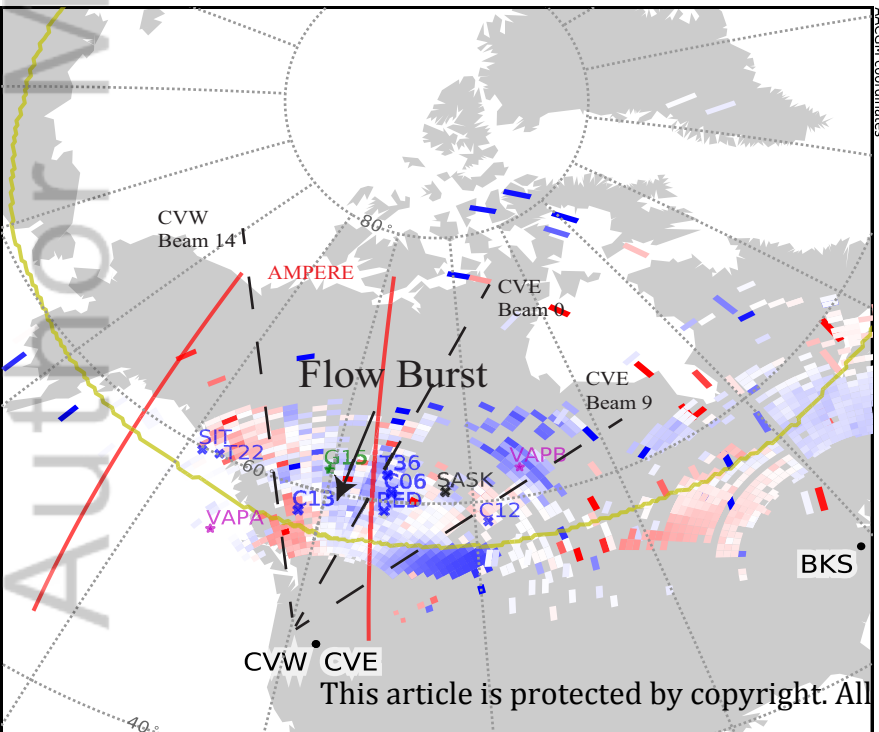
Figure 2.

Author Manuscript

2013-05-18 04:20:00

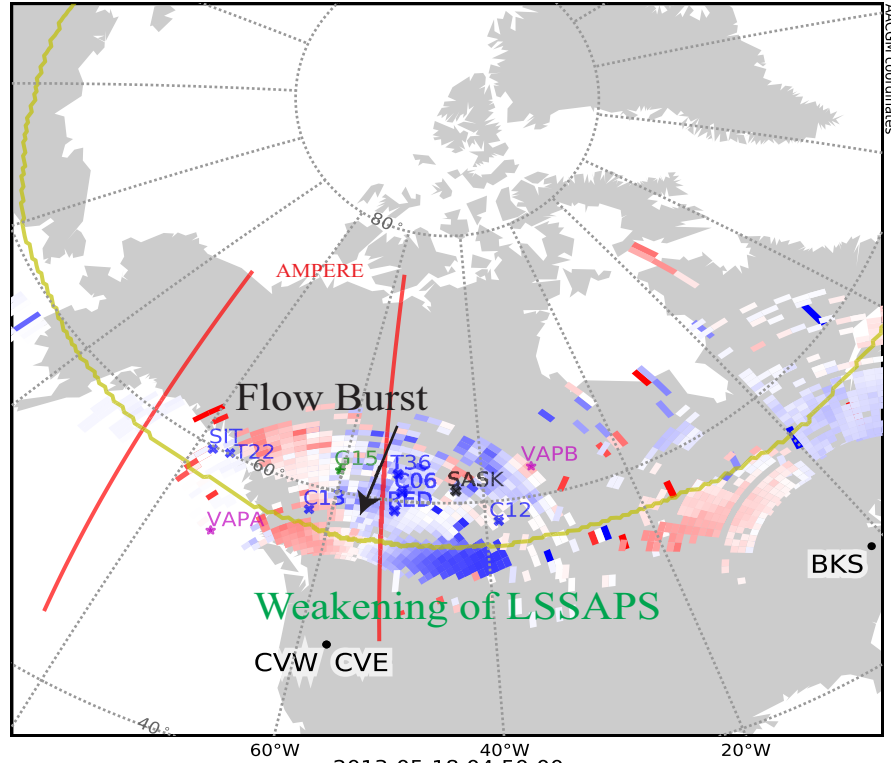


2013-05-18 04:48:00



This article is protected by copyright. All rights reserved.

2013-05-18 04:46:00



2013-05-18 04:50:00

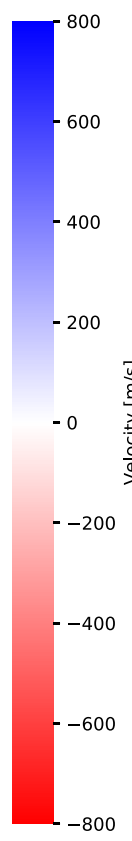
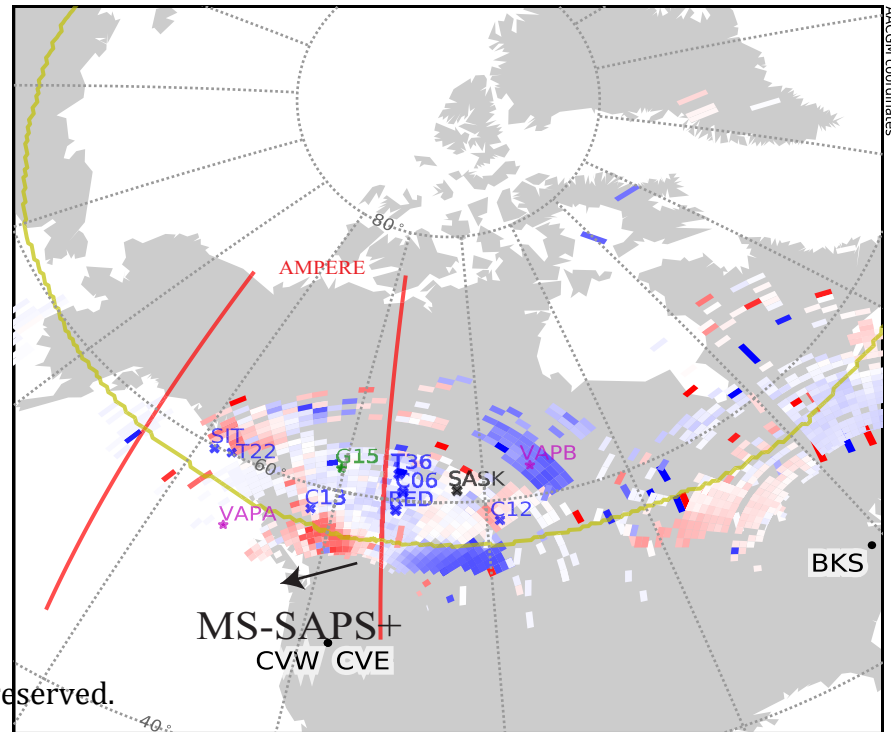
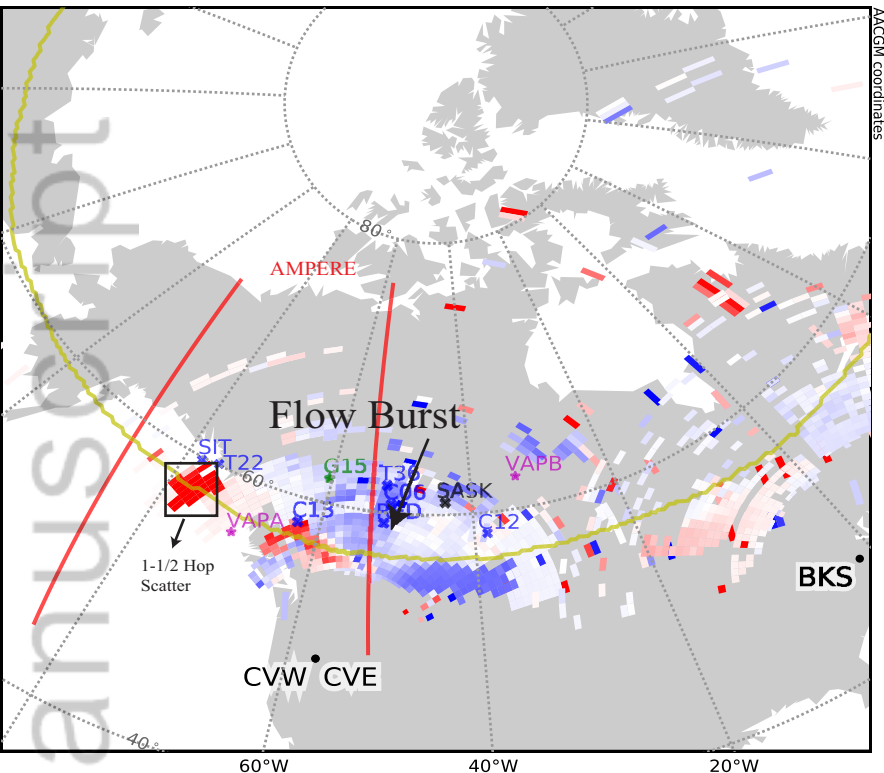


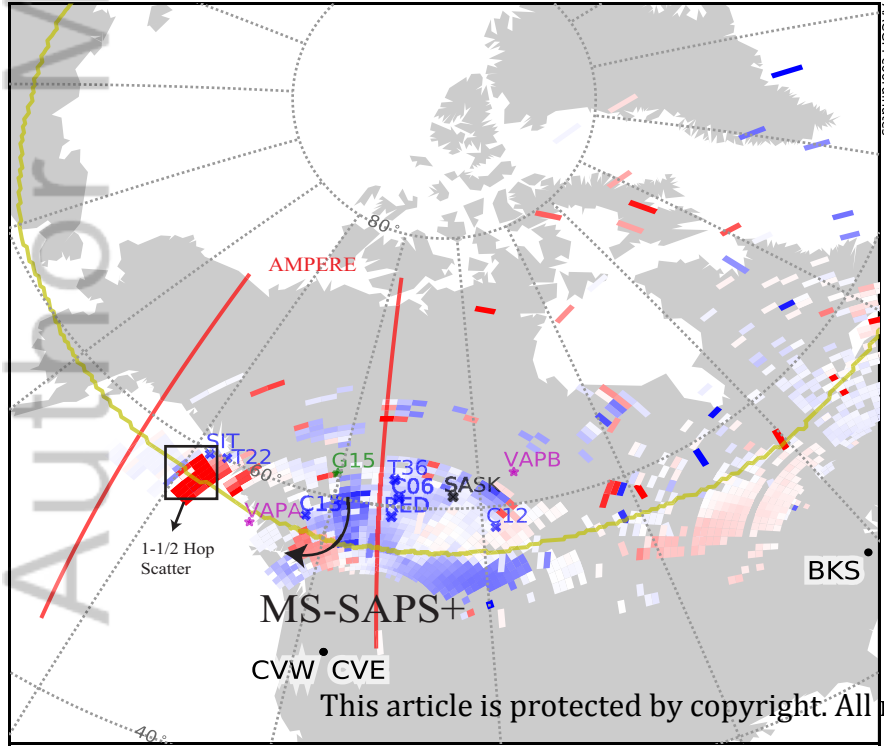
Figure 3.

Author Manuscript

2013-05-18 04:56:00

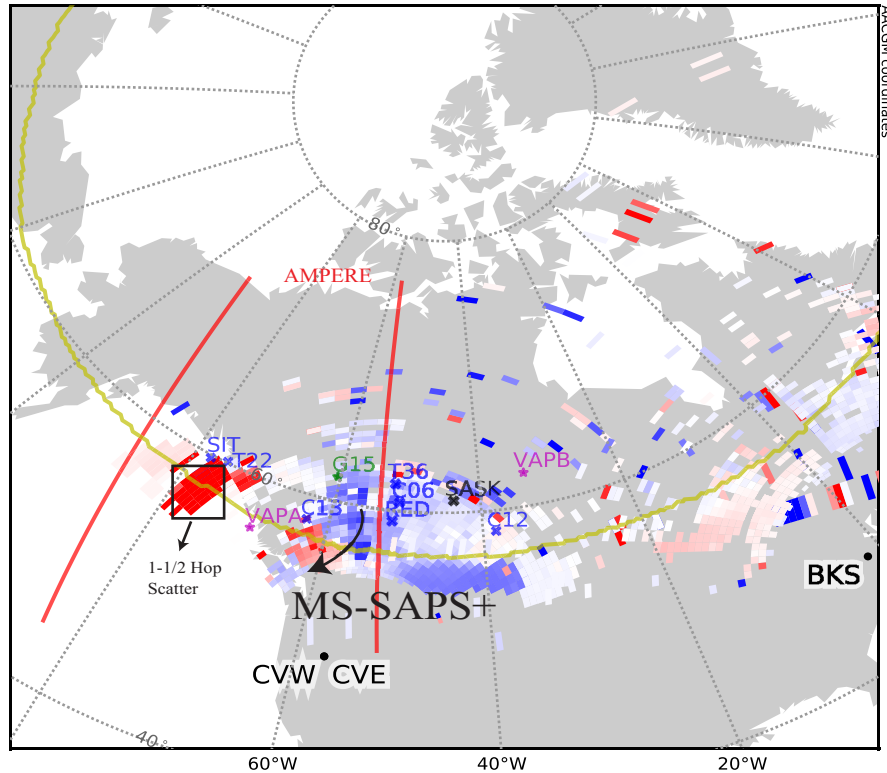


2013-05-18 05:00:00



This article is protected by copyright. All rights reserved.

2013-05-18 04:58:00



2013-05-18 05:04:00

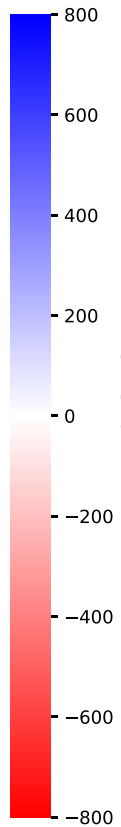
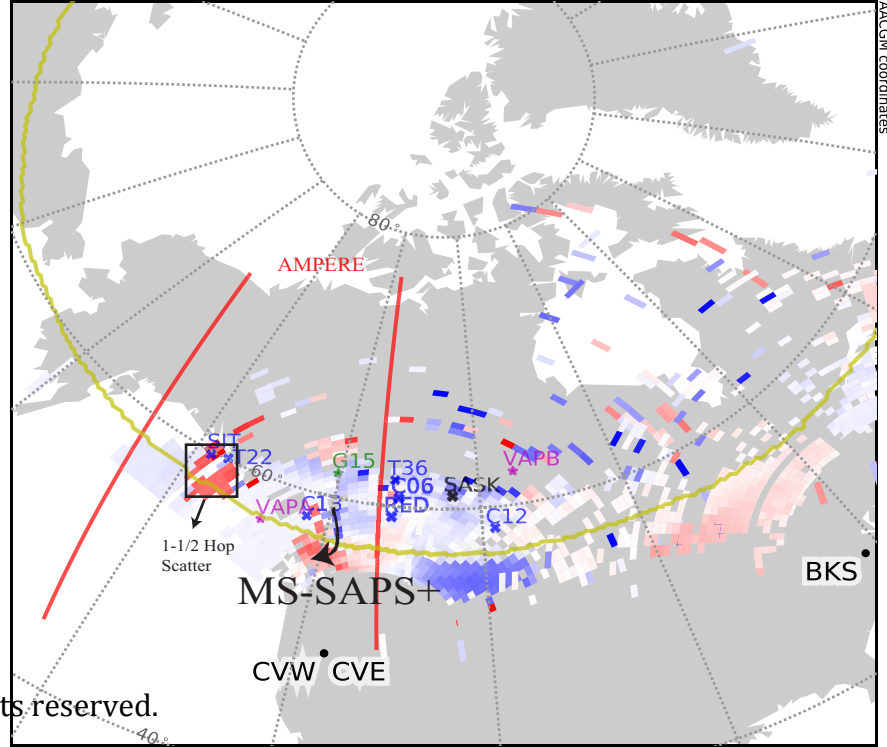


Figure 4.

Author Manuscript

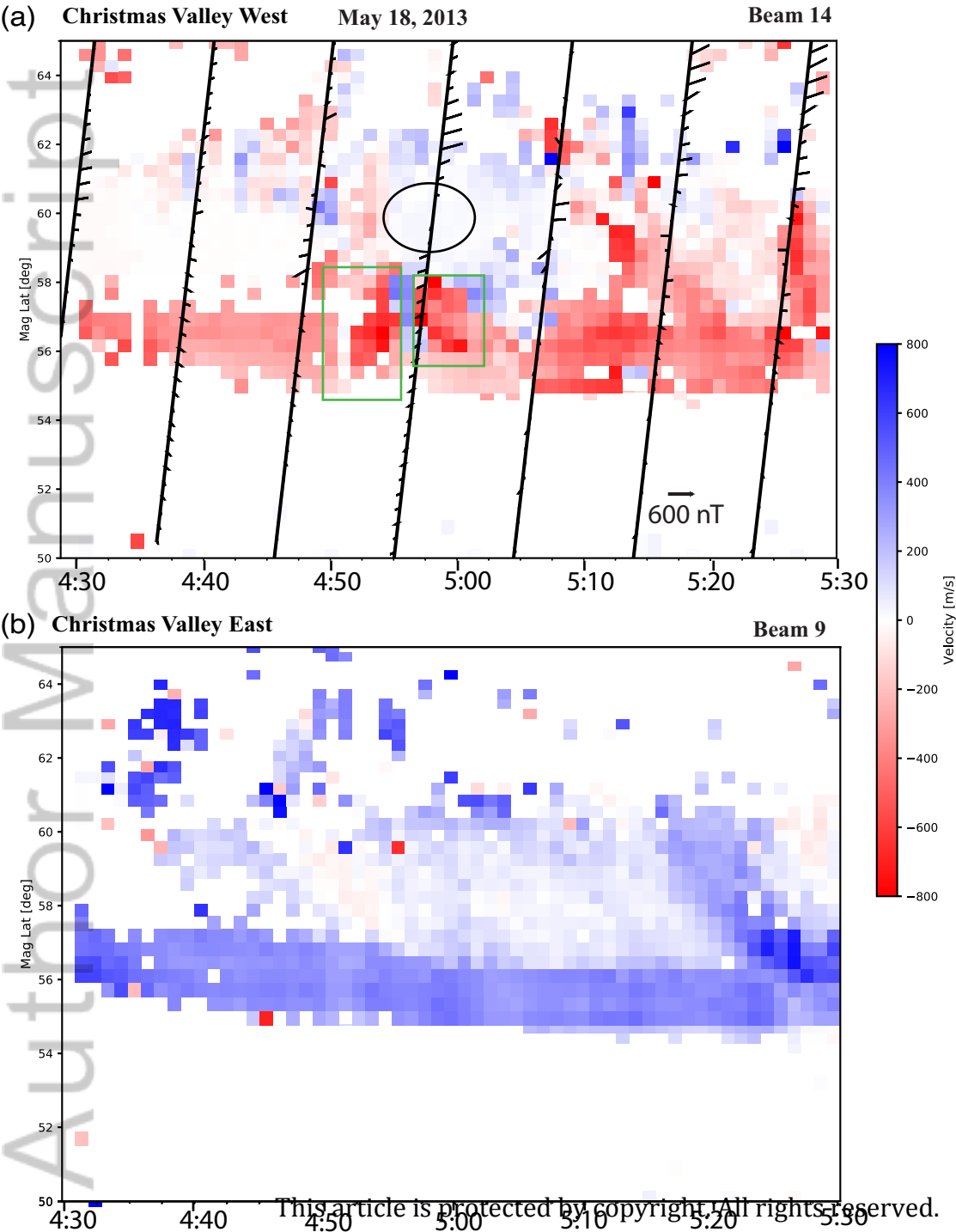
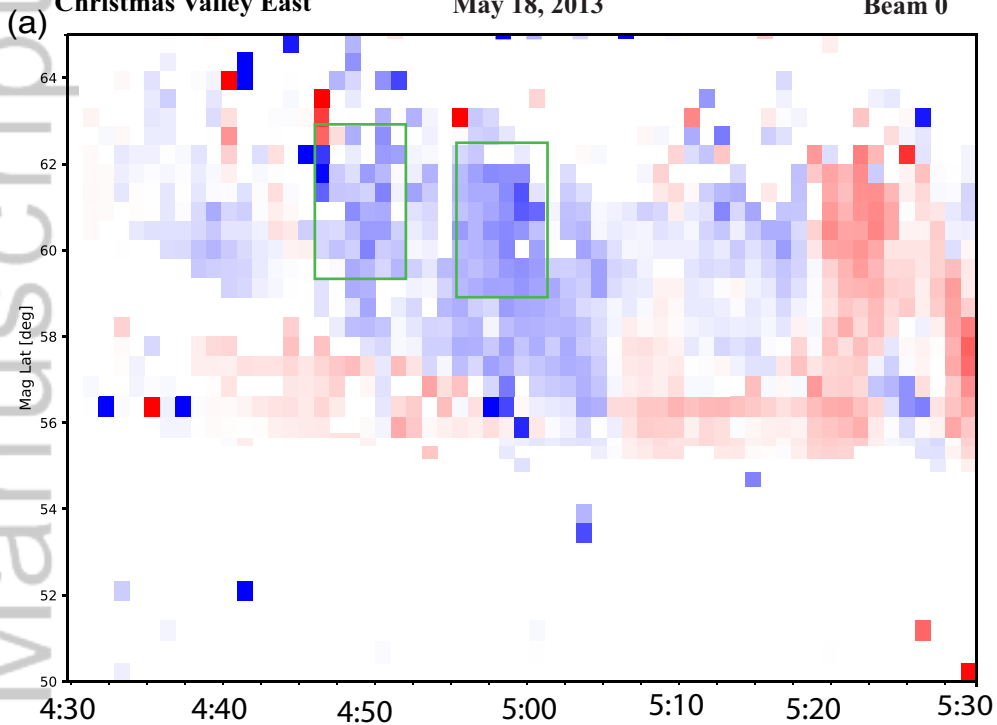


Figure 5.

Author Manuscript



(b) Sask Rainbow 2013-05-18

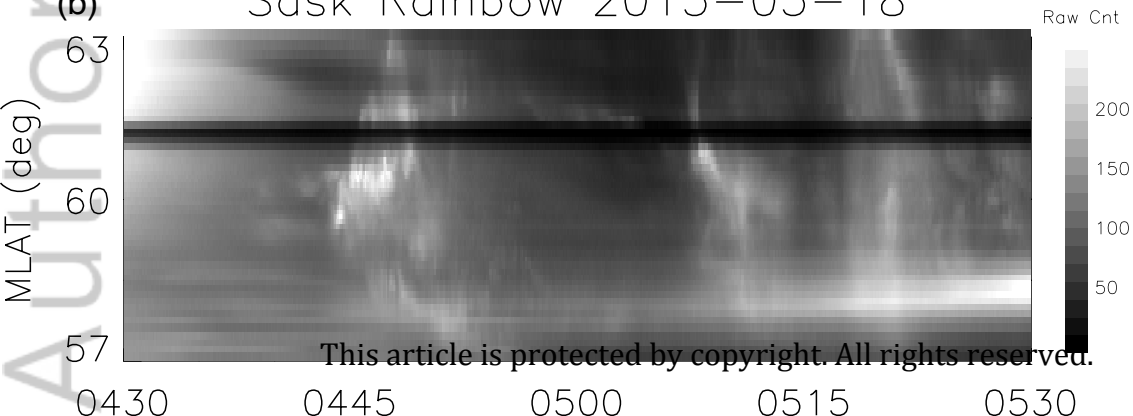


Figure 6.

Author Manuscript

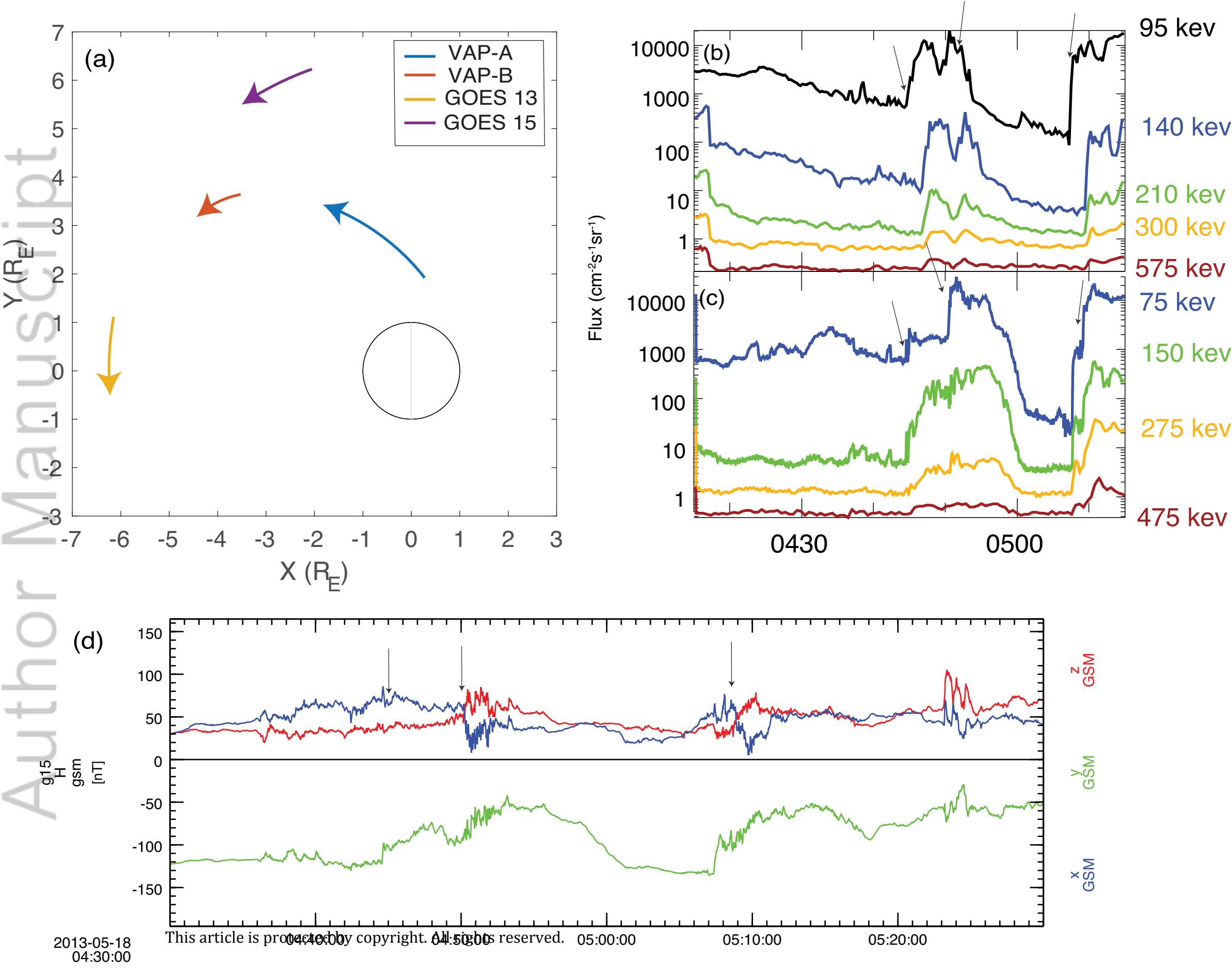


Figure 7.

Author Manuscript

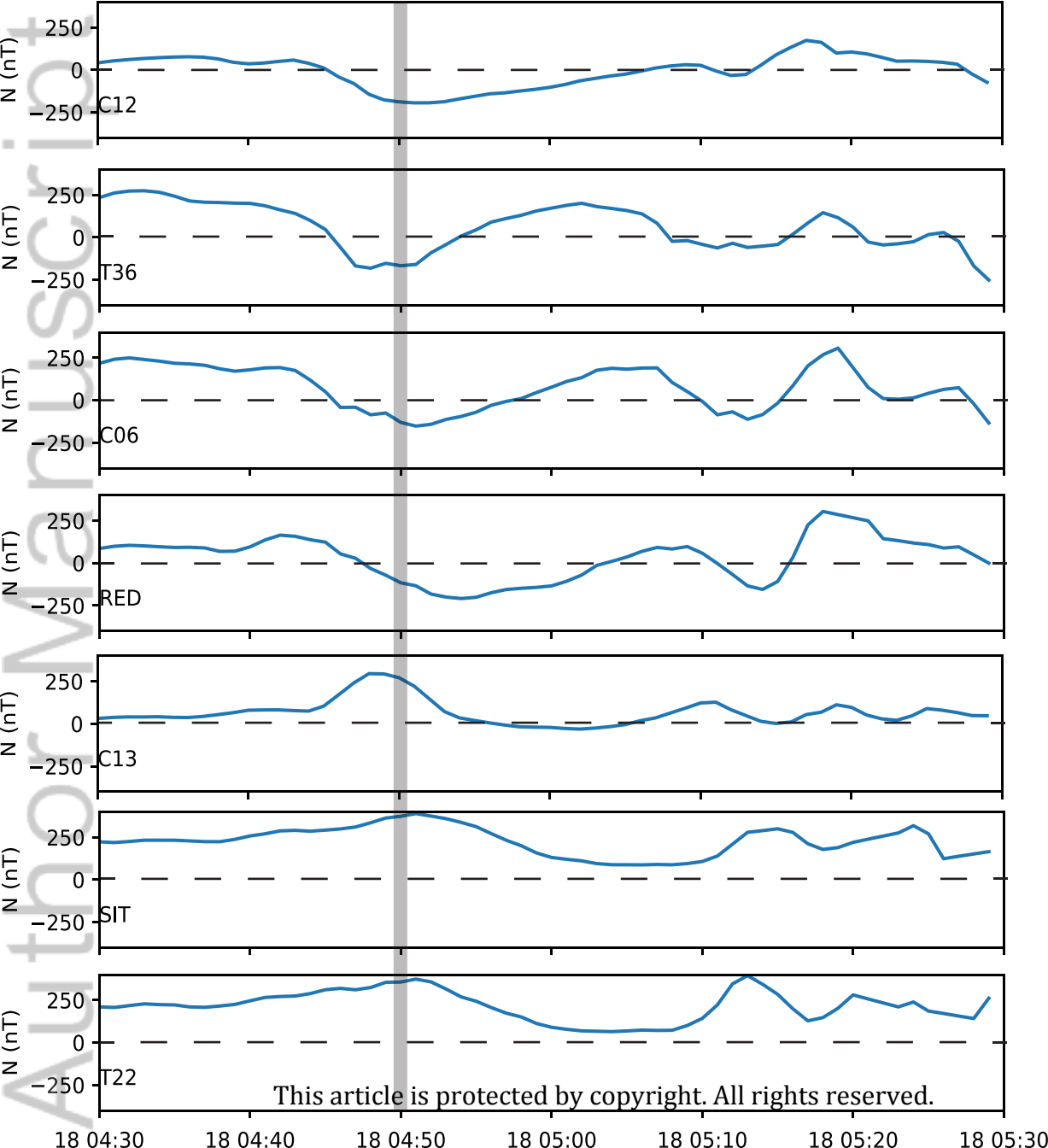
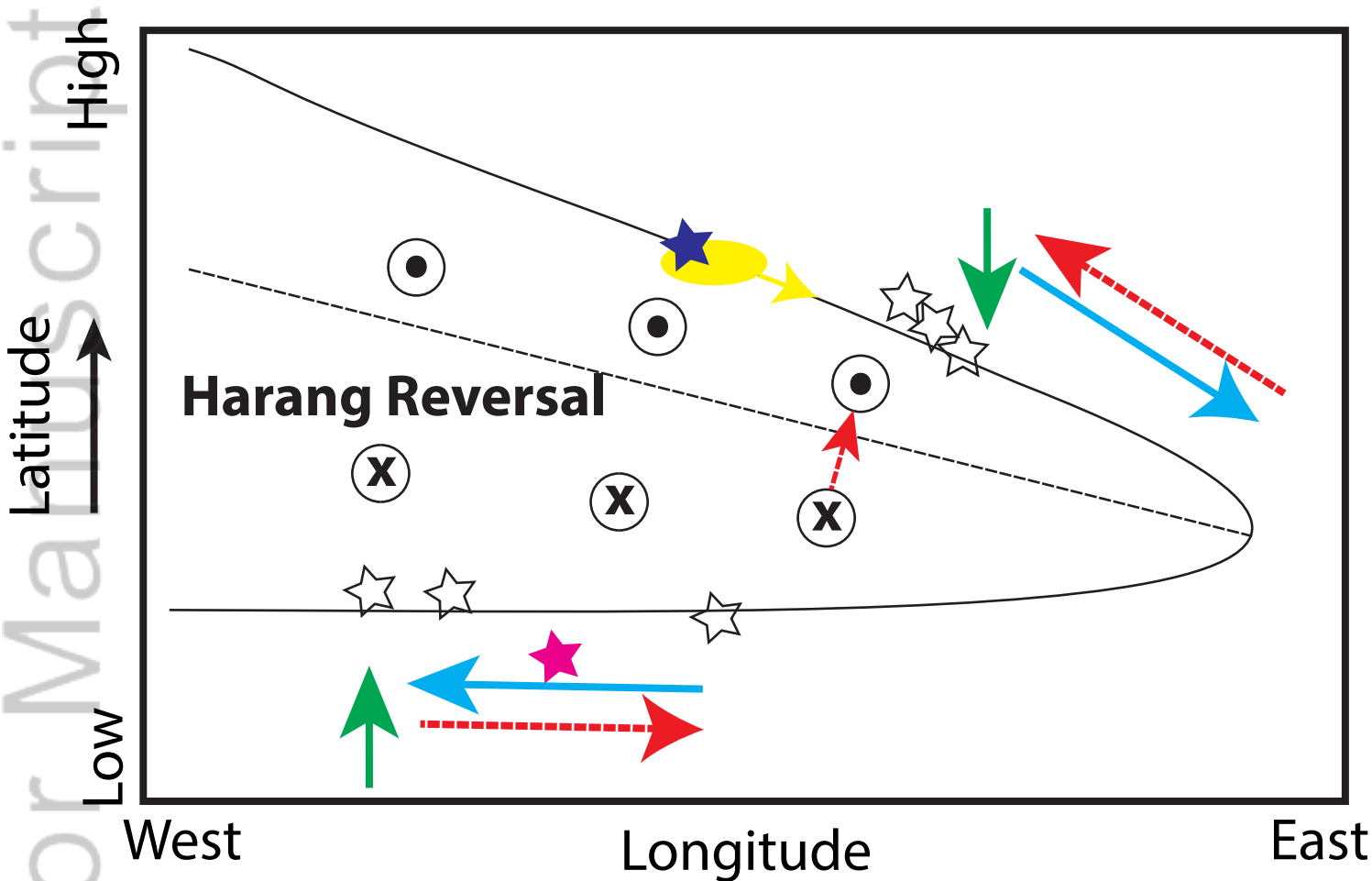


Figure 8.

Author Manuscript



Yellow: Injection

Green: Magnetic Perturbation

Red: Current

Blue: Plasma Flow

Contour: Equipotential Line

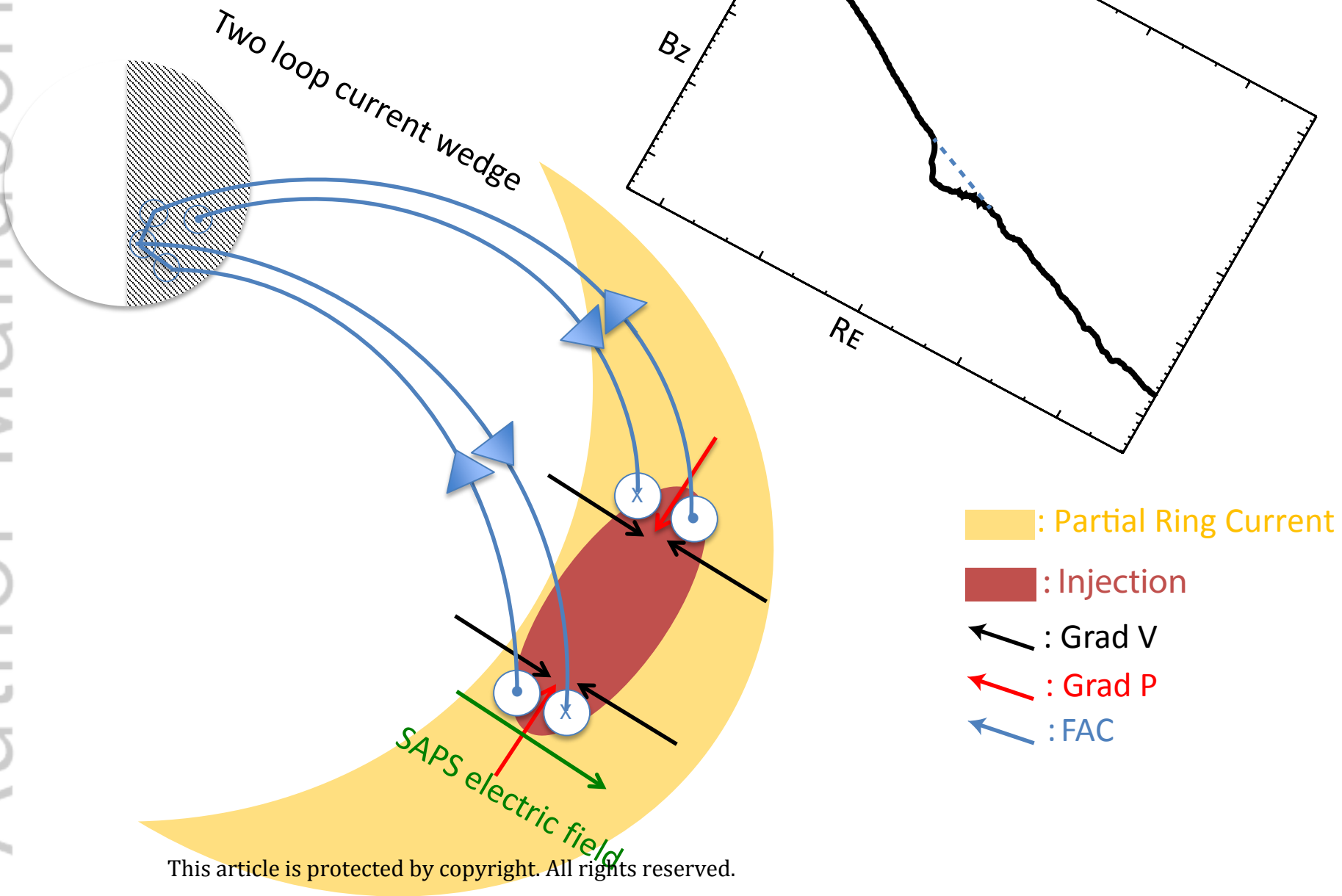
☆ : Magnetometer

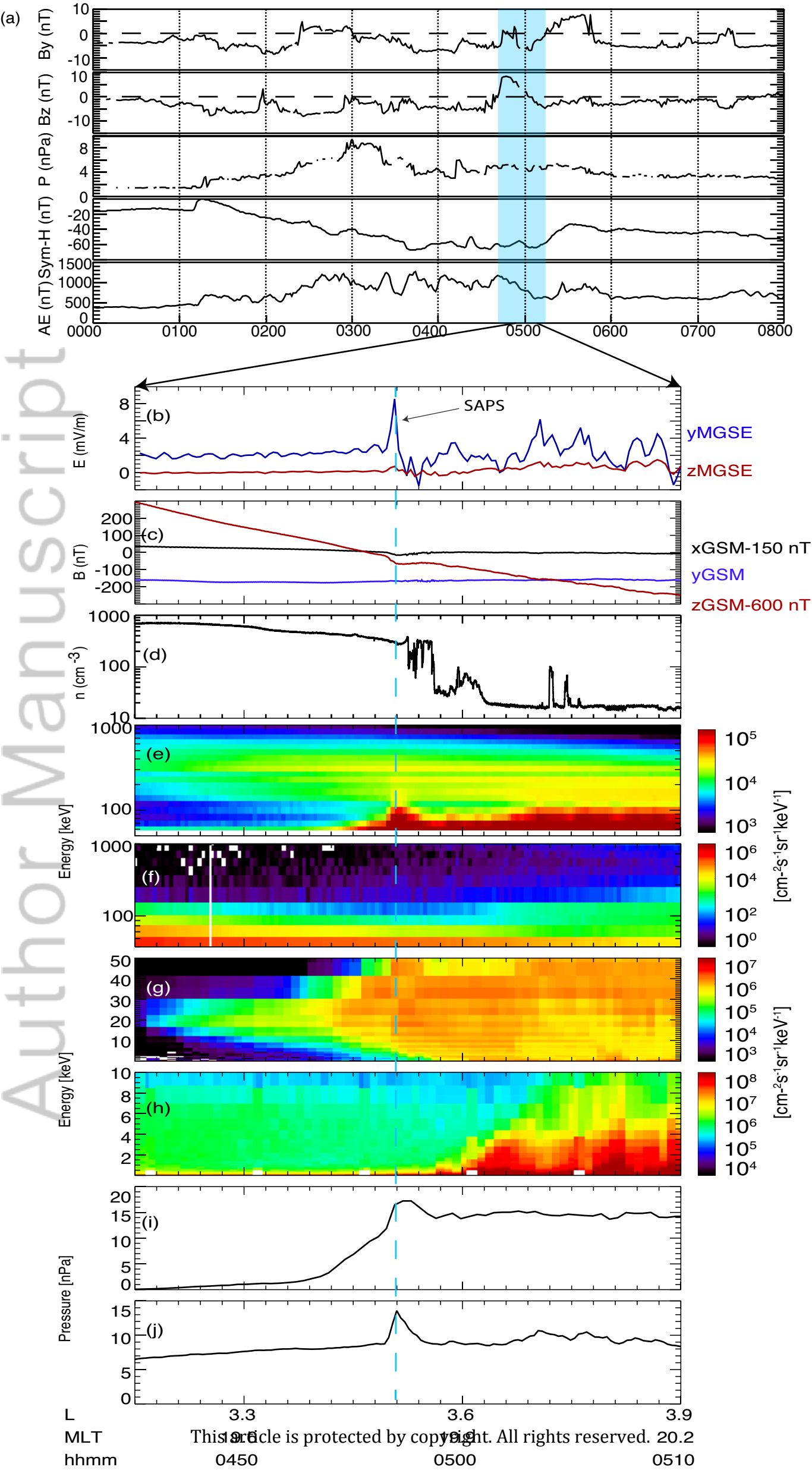
★ : GOES15

★ : VAP-A

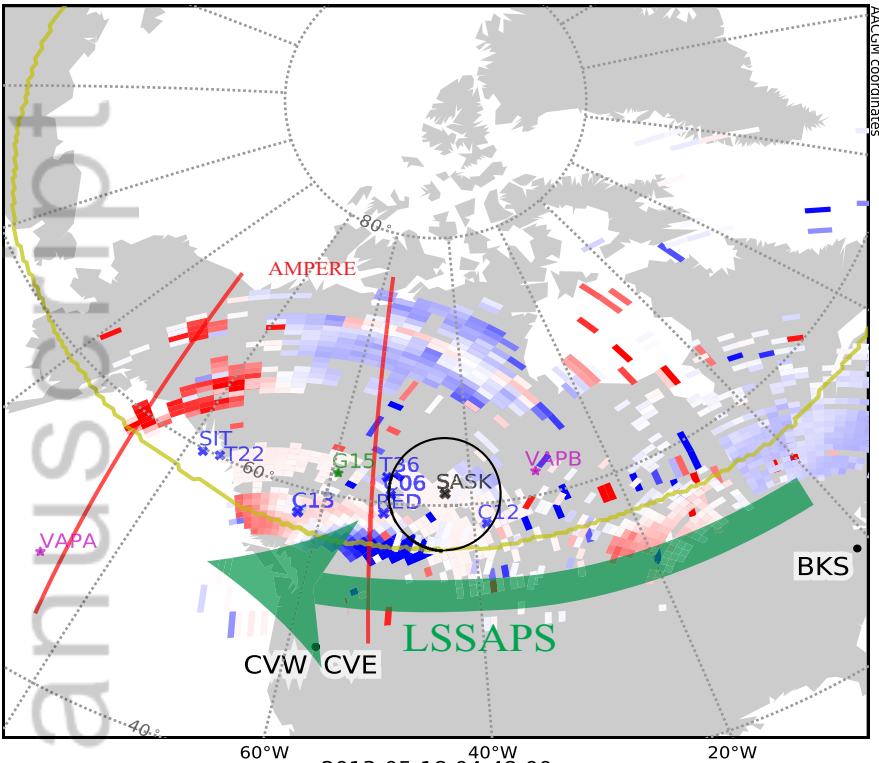
Figure 9.

Author Manuscript



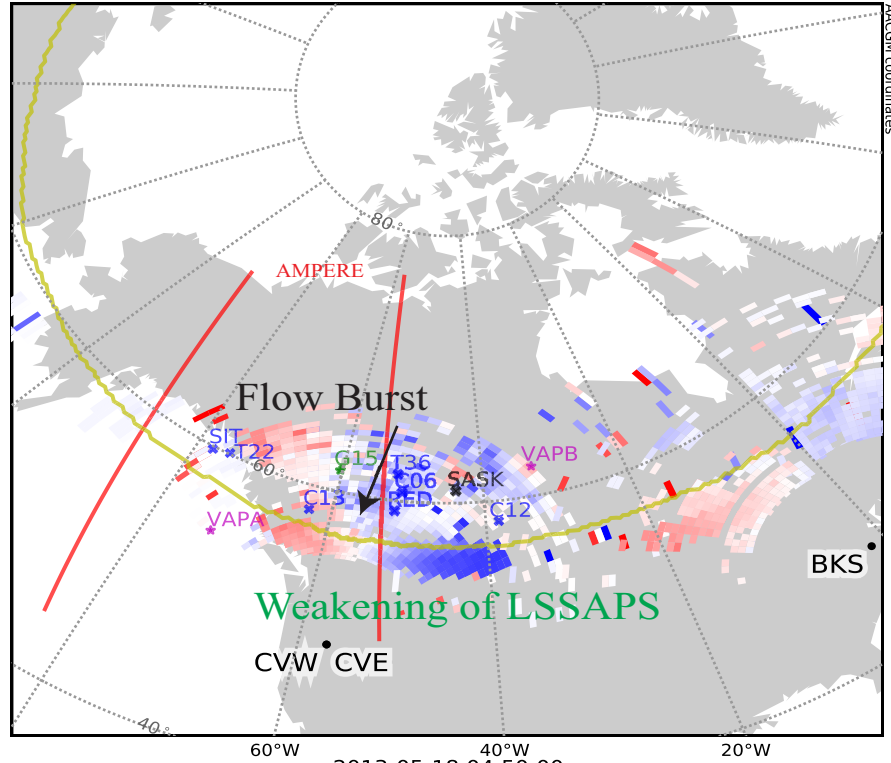


2013-05-18 04:20:00



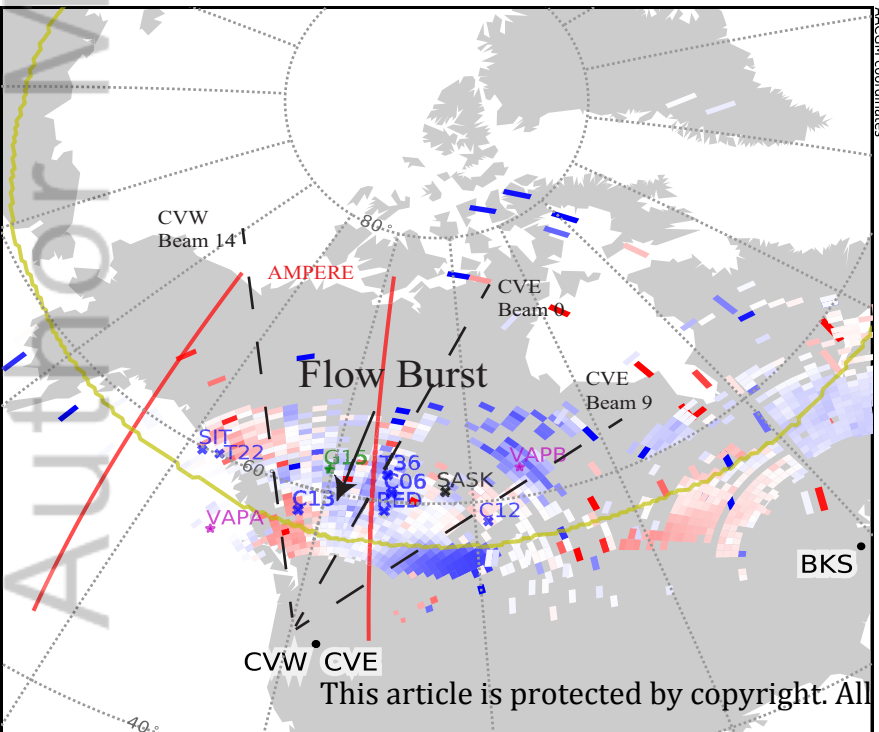
AACGM coordinates

2013-05-18 04:46:00



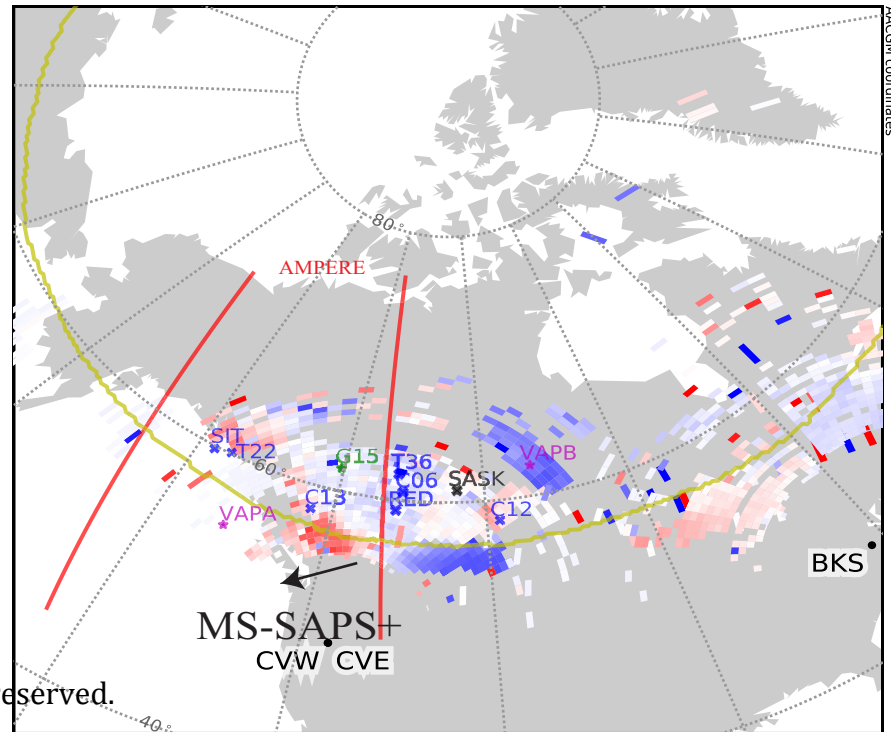
AACGM coordinates

2013-05-18 04:48:00

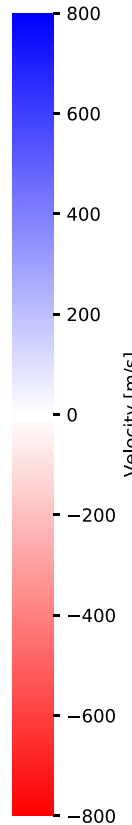


AACGM coordinates

2013-05-18 04:50:00

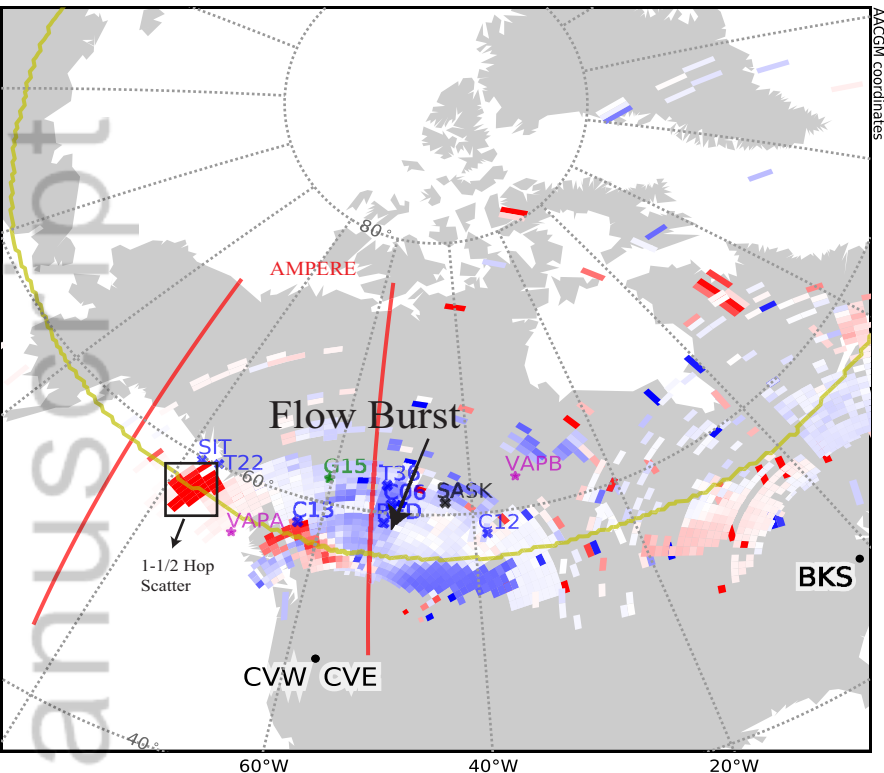


AACGM coordinates

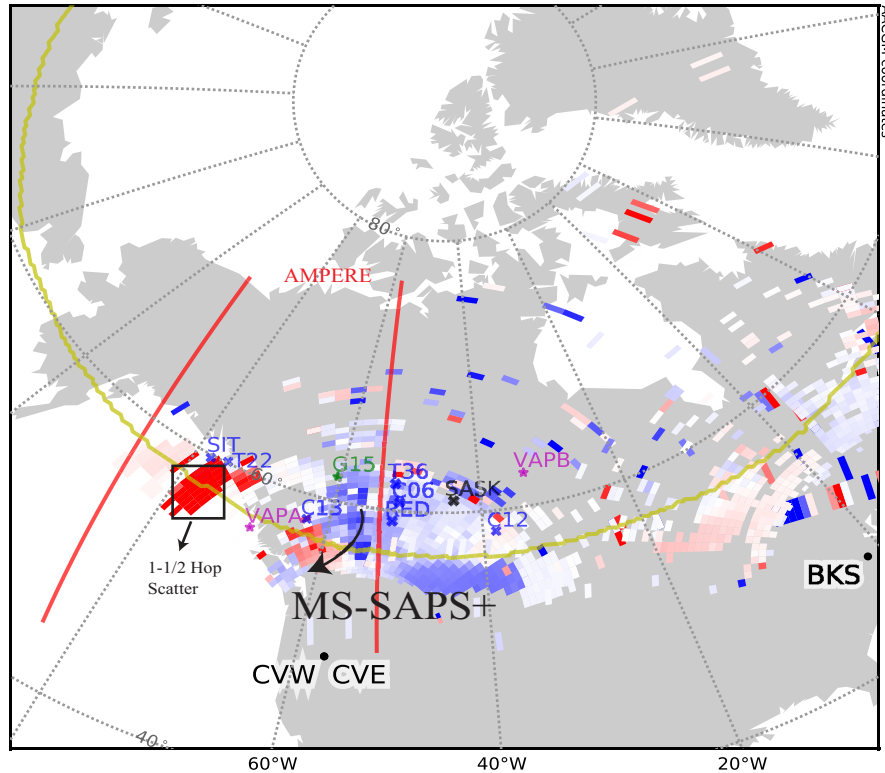


This article is protected by copyright. All rights reserved.

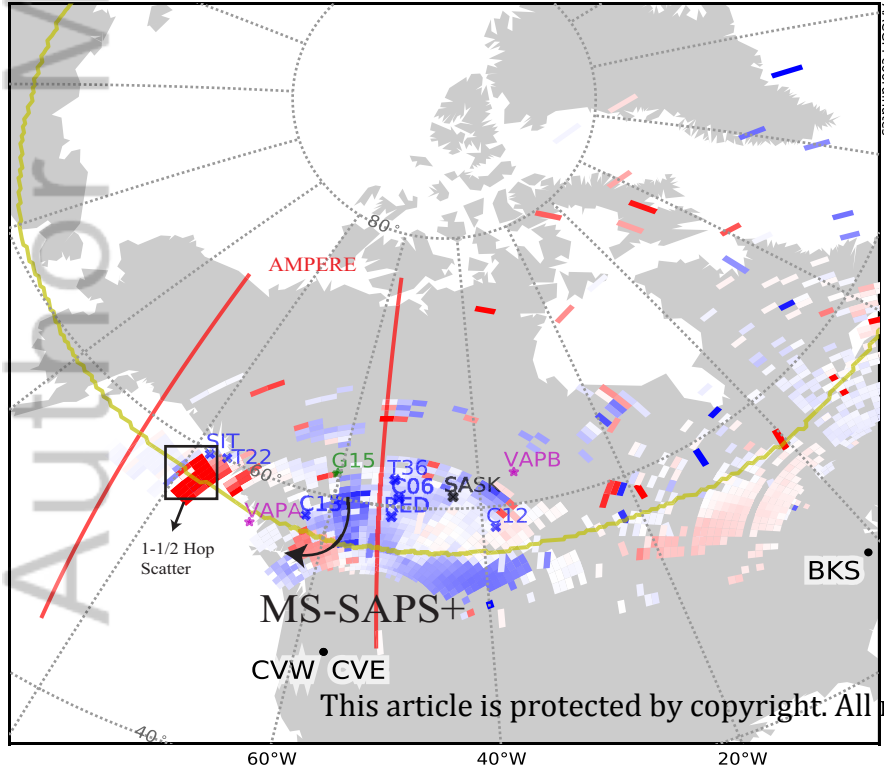
2013-05-18 04:56:00



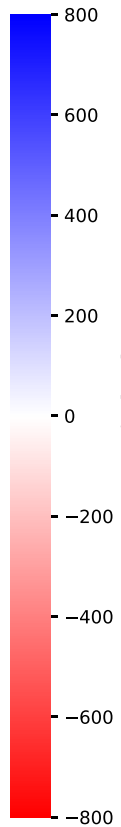
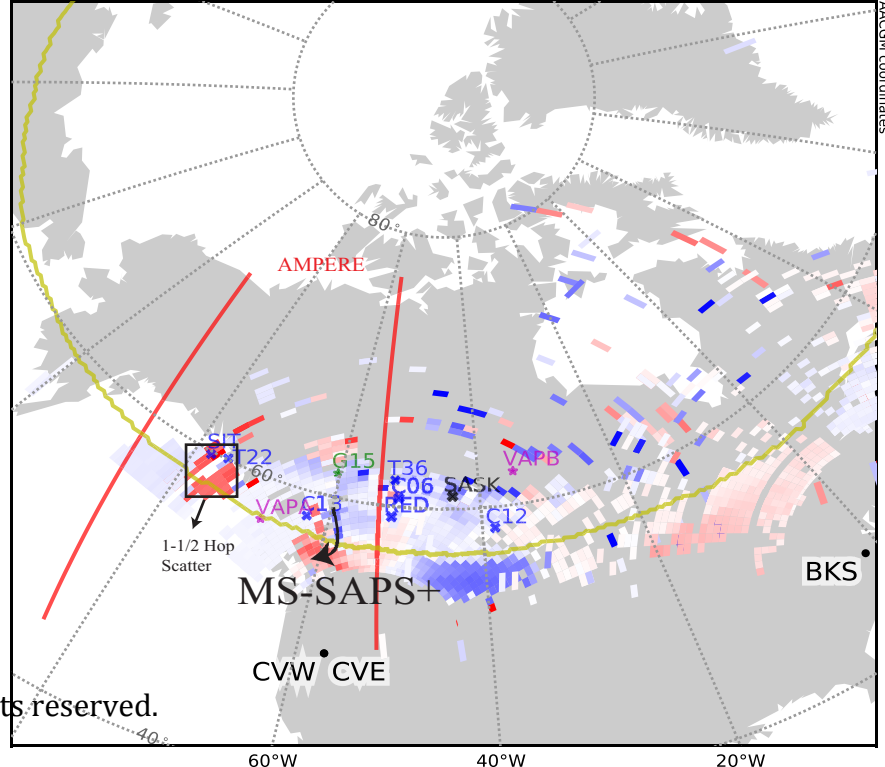
2013-05-18 04:58:00



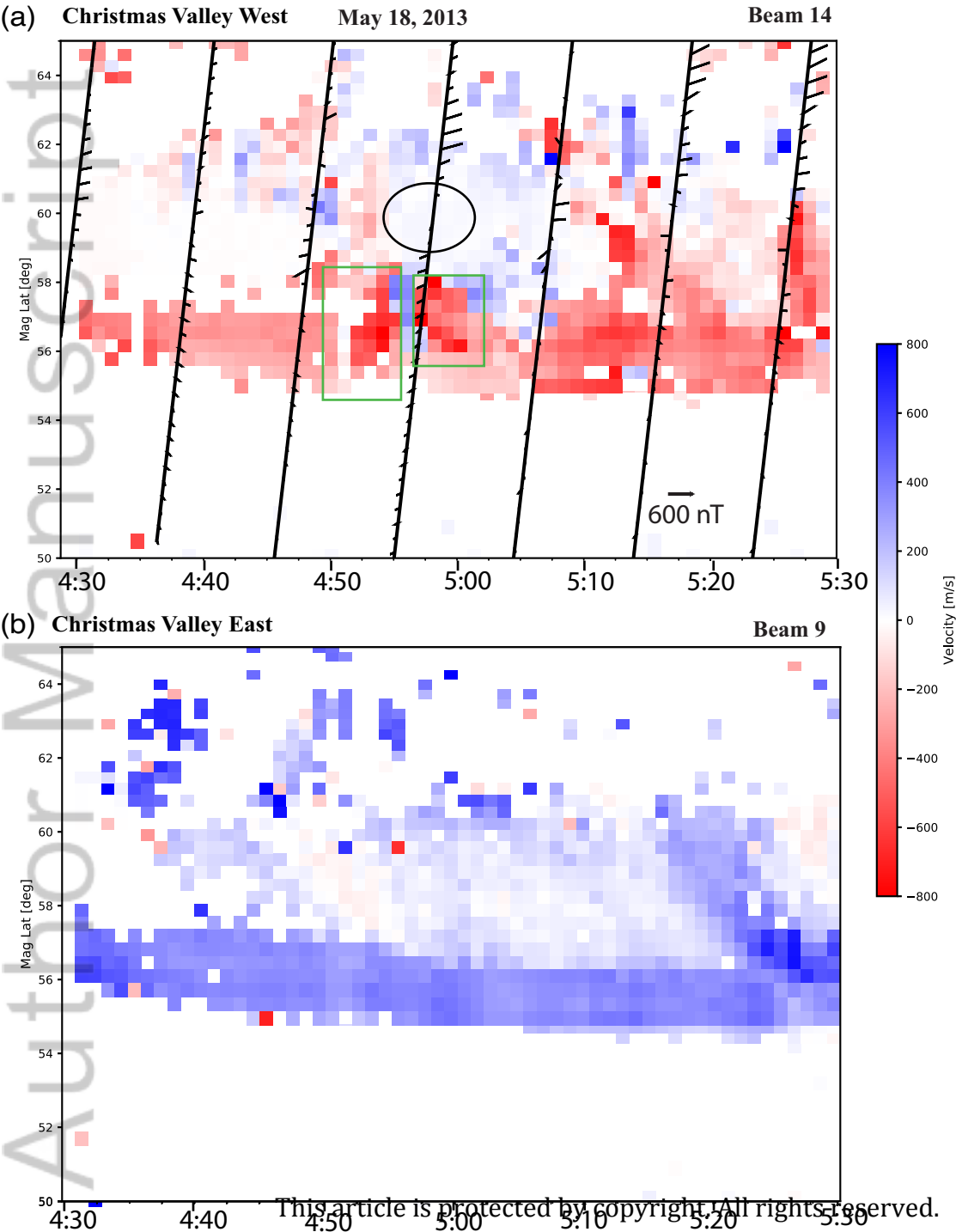
2013-05-18 05:00:00

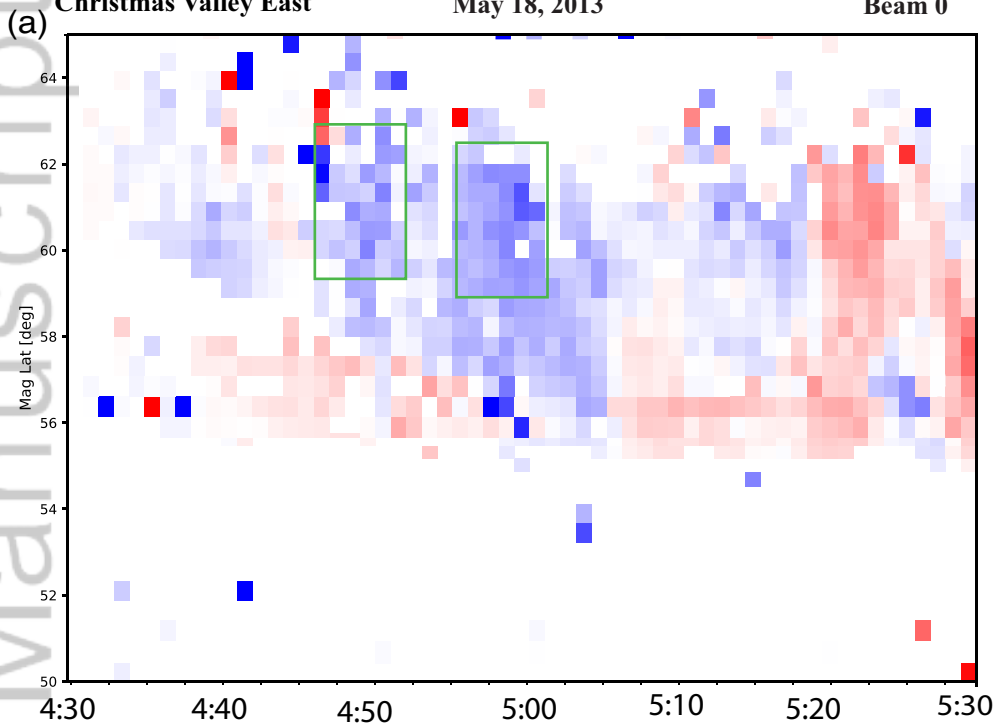


2013-05-18 05:04:00

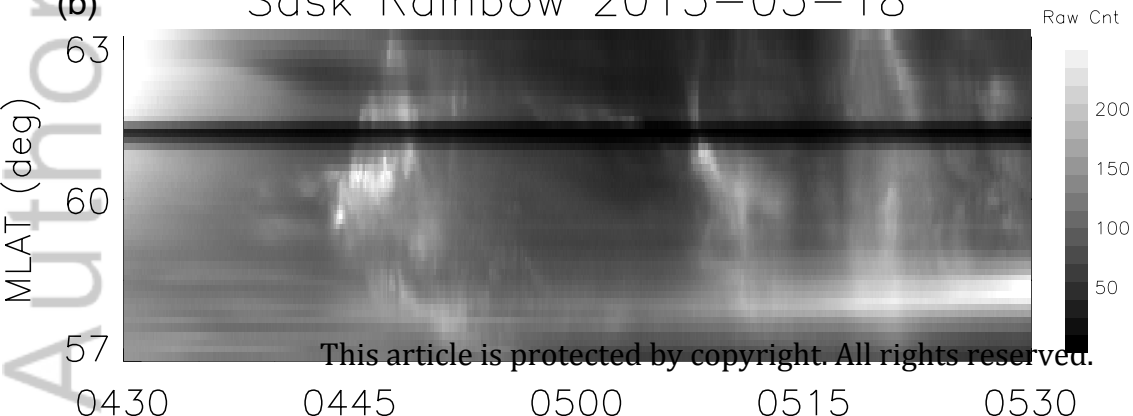


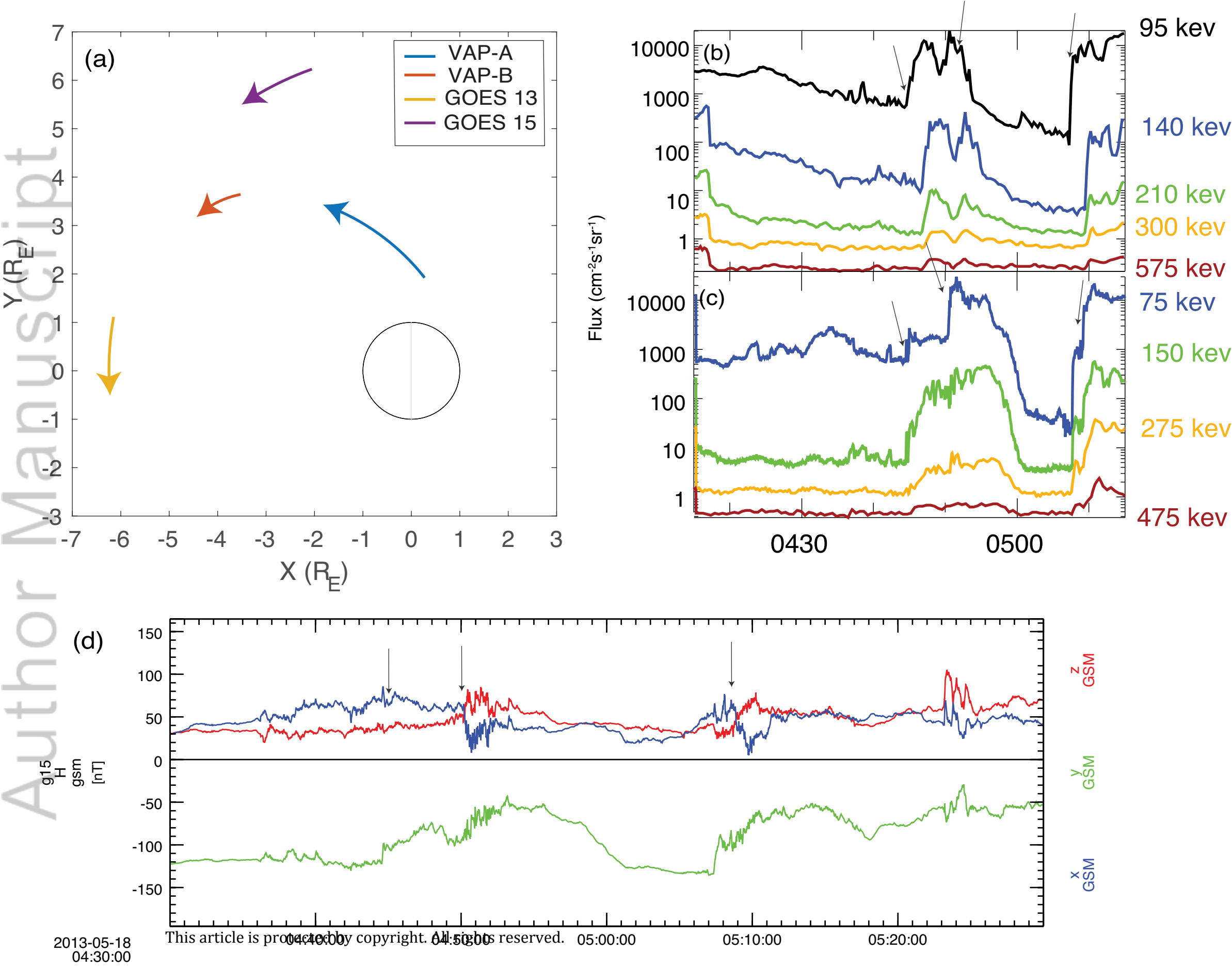
This article is protected by copyright. All rights reserved.

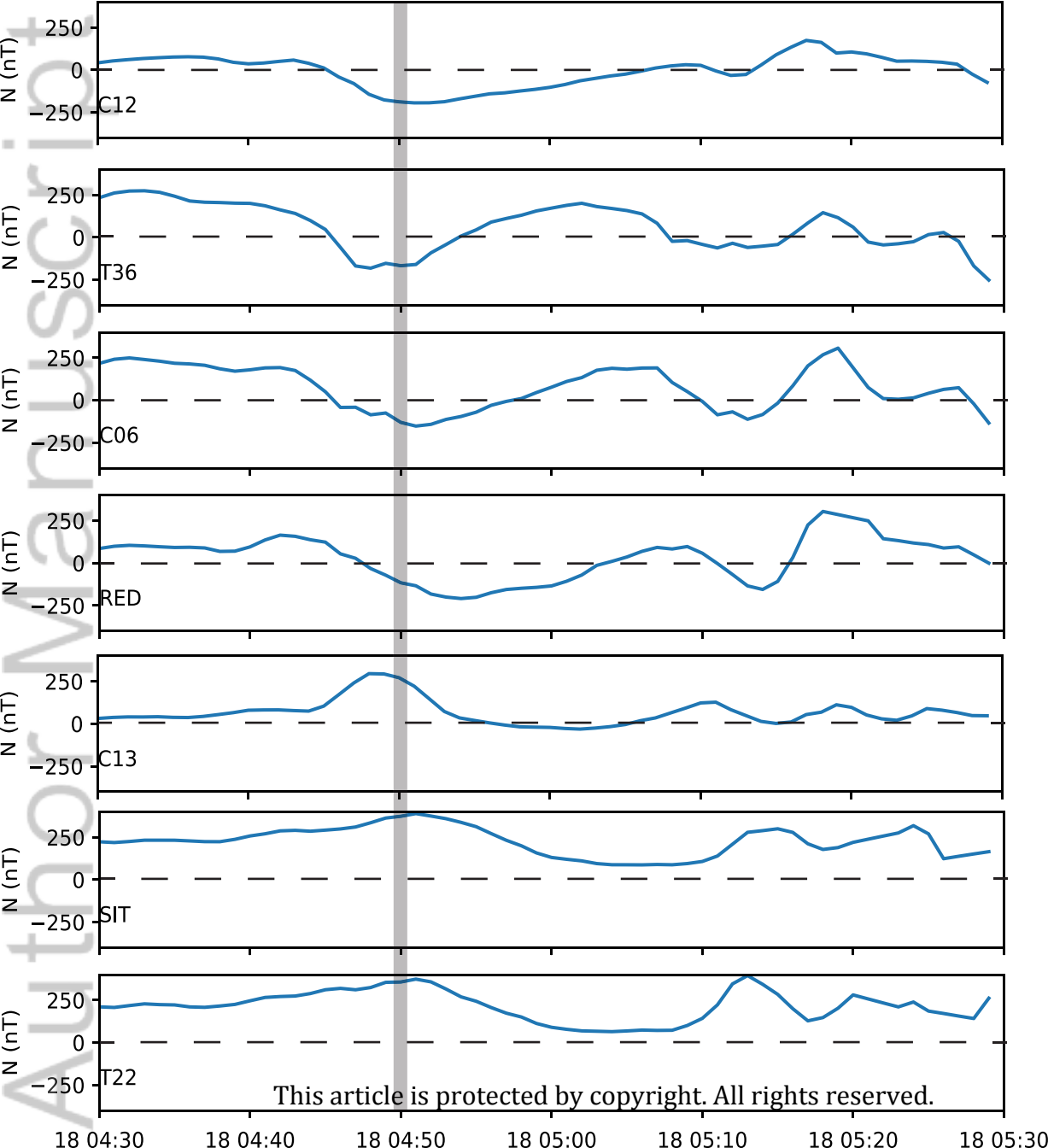


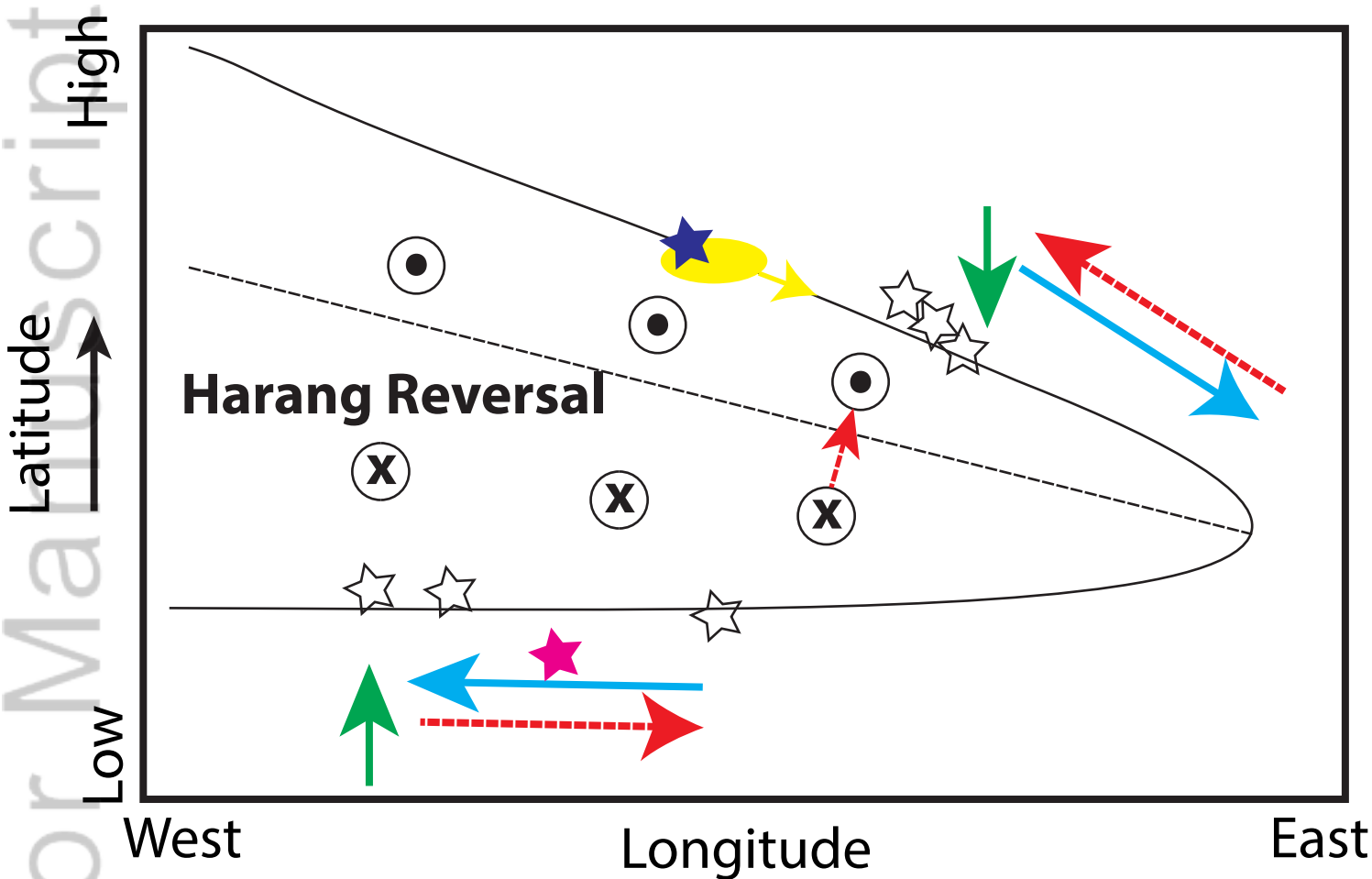


(b) Sask Rainbow 2013-05-18









Yellow: Injection

Green: Magnetic Perturbation

Red: Current

Blue: Plasma Flow

Contour: Equipotential Line

☆ : Magnetometer

★ : GOES15

★ : VAP-A

